EXPLICIT STOCHASTIC SCHEMES FOR TRANSPORT IN PARTICLE-RESOLVED SIMULATIONS

BY

NAKUL NUWAL

THESIS

Submitted in partial fulfillment of the requirements
for the degree of Master of Science in Aerospace Engineering
in the Graduate College of the
University of Illinois at Urbana-Champaign, 2016

Urbana, Illinois

Master's Committee:

Associate Professor Nicole Riemer, adviser
Assistant Professor Taraneh Sayadi
Associate Professor Matthew West

ABSTRACT

Stochastic particle-resolved methods are a recent development in atmospheric aerosol modeling. These methods resolve individual aerosol particles to track the information of their composition during a numerical simulation. This enables the detailed analysis of aerosol and gas phase chemistry, and allows for a more accurate estimate of the aerosol impact on human health and Earth's climate. Transport of all particles in a finite-volume framework can be represented as a stochastic model with each particle having a probability to commute between neighboring grid-cells. This work develops and illustrates the stochastic particle-resolved transport method, which can be used for aerosol transport in atmosphere. The development of the stochastic model was inspired by the passive scalar transport in a predefined velocity field. The model was developed by splitting the transport process into advection and diffusion, and combining them with superposition. Single time-step explicit advection schemes and a Range-kutta numerical scheme were compared to the deterministic advection equation solutions and analytical solutions. The analysis also includes the stochastic modeling of the diffusion process and its results compared to analytical solution. For all cases, a quantification of total error and a numerical convergence analysis is presented.

To my brother, Aanchi, and my parents, for their love and support.

ACKNOWLEDGMENTS

I have had a distinct privilege of working with my adviser Professor Nicole Riemer and would like to express my sincere gratitude for giving me this opportunity to work on this project. Her wise guidance and valuable lessons were well appreciated during the course of this work. I am also grateful to her for supporting me financially during this project. I want to thank Professor Matthew West for co-advising this project, and for providing his continuous support and insights on this work. Without professor West's continuous input on the project, this work would not have been possible. This work has been one of the greatest learning experience of my life.

I am thankful to my graduate colleagues, Jeffery Curtis and Micheal Hughes for providing helpful feedbacks and constructive suggestions in writing the first chapter of this thesis. I am thankful to my friends Suraj Bansal, Yashwanth Kumar and Sandeep Murthy for enduring this journey with me.

I will be forever grateful to my papa and maa for believing in me and providing me with endless motivation and support since the time I first understood basic arithmetics.

I also want to thank Professor Taraneh Sayadi for co-advising my thesis. Last but not the least, I also want to thank Atmospheric System Research Program of the Department of Energy for funding the research and providing me with this wonderful opportunity.

Thank you all for your encouragement and support.

TABLE OF CONTENTS

LIST OF FIGURES

LIST OF ABBREVIATIONS

WRF	Weather Research and Forecast
PDE	Partial Differential Equation
FBPT	Flux Based Particle Transport
PST	Passive Scaler Transport
FV	Finite-Volume
FV-PST	Finite-Volume Passive Scaler Transport
PM	Particulate Matter
RMS	Root Mean Square
S	Stochastic
adv	Advection
diff	Diffusion

LIST OF SYMBOLS

i	Grid-cell number in x direction
j	Grid-cell number in y direction
k	Time-step number
n	Number of particles analytical solution
q	Passive scalar analytical solution
u	Velocity magnitude
D_0	Diffusion Coefficient
N_i^k	Number of particles in grid-cell i at time-step k
Q_i^k	Specie concentration from Finite-volume solution to scalar transport equation(PST) in grid-cell i at time-step k.
V	Sample Volume
${Q_{\text{part}}}_i^k$	Particle concentration from Stochastic algorithm (FBPT) in grid-cell i at time-step k
F	FV flux term
G	FBPT flux term
$[(P)_i]_{+\text{x}}$	Probability of a particle in cell i to move to grid-cell in +x direction
C_{u}	Advection Courant number
C_{d}	Diffusion number
e_i^k	Absolute Error in grid-cell i at time-step k

CHAPTER 1

INTRODUCTION

Suspended particles in a fluid are the focus of many fields in science and engineering. Among various phenomena such as reaction, growth and deposition, occurring to the particles, transport due to fluid movement is an important aspect in various practical applications such as biological particle movements [Resat et al., 2009], computer graphics [Müller et al., 2003] and atmospheric pollutant movements [Riemer et al., 2009, Zaveri et al., 2008, 2010]. The numerical method discussed in the thesis is particularly applicable to the transport of atmospheric pollutants, such as aerosols in the atmosphere.

1.1 Atmospheric Aerosol particles: Life-cycle and Impacts

An aerosol is a colloidal solution of liquid droplets or solid particles in a gas phase. For atmospheric aerosols the gas phase is air. Atmospheric aerosol particles are emitted by natural or anthropogenic sources. The type of aerosols emitted vary spatially around the world. For example, mineral dust aerosols are abundantly found near desert regions such as Sahara, while sea salt aerosols are primarily found over the oceans. Based on the process how they were brought into the atmosphere, aerosols are commonly classified as primary and secondary aerosols. More on this classification is described in the following section.

Atmospheric aerosol particles are composed of sulphates, nitrates, ammonium, black carbon, complex salts and other compounds [Huebert and Lazrus, 1980]. Figure 1.1 shows a sample of aerosol particles with different compositions. Since the shape of aerosols is often irregular, the size of aerosols can quantified by mean diameter of a volume equivalent sphere. The mean diameter of aerosol particles ranges from 1 nm to 10 mm [Jacobson

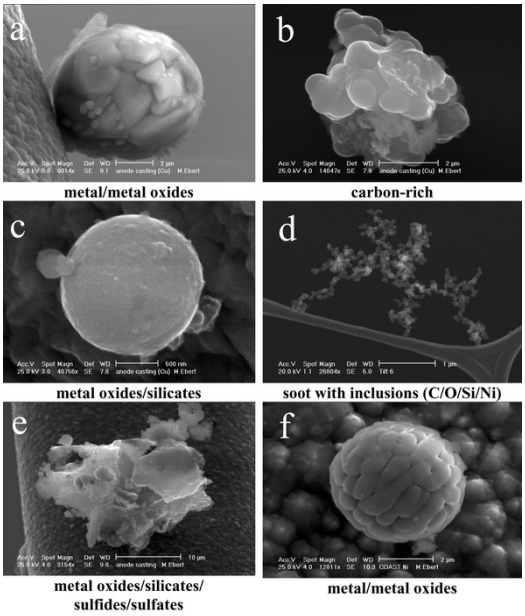

Figure 1.1: Composition of different aerosol particles[Jacobson Chapter 5, 2012].

Chapter 5, 2012]. The aerosols are classified into different modes based on their size. Figure 1.2 shows three primary modes (1) Aitken mode ($PM_{2.5}$), (2) Accumulation mode ($PM_{2.5}$) and (3) Coarse particle mode, based on the size distribution of aerosols. Atmospheric aerosol particles with the diameter larger than 100μm are very rare.

Aerosols also vary widely in shapes. Incomplete combustion from vehicles leads to the complicated shaped aerosols like fractals, while some aerosols, such as hygroscopic aerosols, are spherical in shape. Previous works have shown that the non-spherical nature of aerosols introduces relevant differences in optical properties of aerosols [Pilinis and Li, 1998] and shape can be a relevant variable in numerical models for accurately estimating the impacts of aersosol particles [Adachi et al., 2010]. Since the focus of the particle-resolved models is on resolving particle composition rather than their shapes, and the numerical model included in this work focuses on particle transport assuming the shape of all aerosol particles to be spherical.

1.1.1 Life-cycle of Aerosols

The life-cycle of aerosol particles starts with the generation (or emission) from various sources. Primary aerosol particles are directly emitted in the form of liquids or solids from sources like incomplete combustion of fossil fuels, deserts and plant fragments. Secondary aerosol material is formed from gaseous precursors from various sources. The secondary aerosol particles can be formed either by the volatile materials such as SO_4 reacting in the air to form low-volatility gas species (sulfuric acid, H_2SO_4), which can convert into a liquid particle state or by condensation of the gas species on already existing primary or secondary aerosol particles. After formation or emission of the aerosols, these particles undergo aging, which involves the physical processes of coagulation, condensation of non-volatile materials on aerosols (like sulfuric acid) and the chemical aging processes of photochemical aging. Removal of aerosol particles from the atmosphere happens with the removal processes, such as washout and dry-deposition [Jacobson Chapter 5, 2012]. A schematic for the life-cycle of aerosols is given in Figure 1.2, from Whitby and Cantrell [1976]. Typical time scale for aerosol particles' life-cycle in atmosphere is of the order of two weeks [McCarthy, 2001].

1.1.2 Impacts of Aerosols

Aerosols have a significant impact on the environment and human health. Impacts of aerosols are commonly classified as (1) health effects, (2) direct effects on climate and (3) indirect effects on climate.

Small aerosol particles ($PM_{2.5}$) are found to be lethal to human health. Aerosols are responsible for lung cancer, chronic obstructive pulmonary disease (COPD) and transport of other airborne diseases [Pope III et al., 2009]. According to Pope III et al. [2009], 10 $\mu g/m^3$ of $PM_{2.5}$ aerosols for long periods of time reduces the human life expectancy by 5 to 10 months.

Since aerosols can reflect, scatter and absorb light coming from the sun, optical properties of aerosols are relevant in the direct effects of aerosols on climate. The ability of absorbing and scattering light depends of the size and composition of the aerosols. The size range of some aerosol particles is of the order of the wavelength of visible light. This enables the aerosol particles to scatter and absorb solar radiation and affect the radiation budget of Earth.

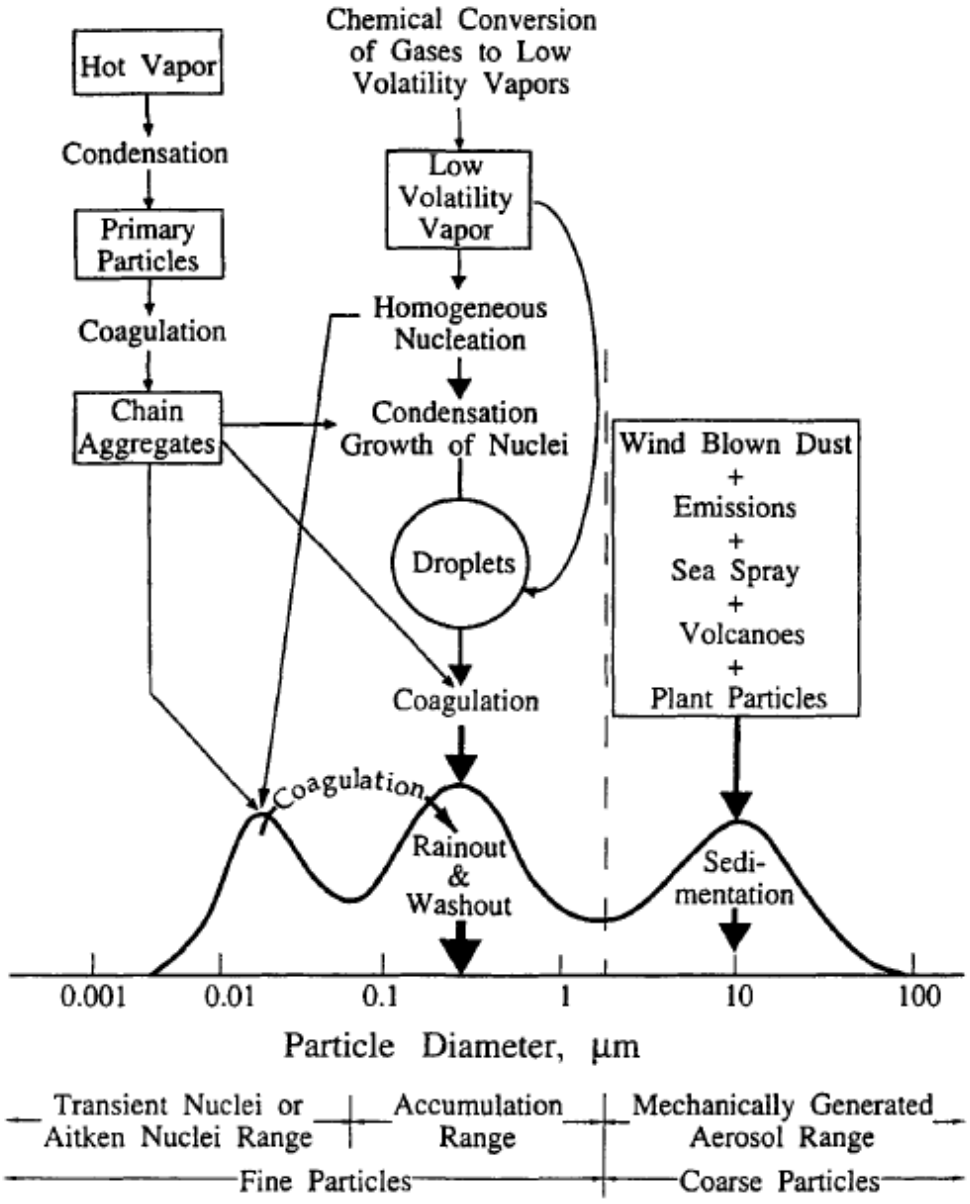

Figure 1.2: Principal modes, sources, and particle formation and removal mechanisms [Whitby and Cantrell, 1976]. Image is taken from Seinfeld and Pandis [2012].

The composition also affects the radiation effects of aerosols. Some aerosol species, such as carbonaceous compounds, absorb visible light while other species, such as sulfates and nitrates, do not. Optical absorption properties of aerosols have been studied extensively in various regions around the world [Bergstrom et al., 2007, Chung and Seinfeld, 2005, Yang et al., 2016]. These absorbing and scattering effects are some of the direct effects of aerosols on Earth's radiation budget.

The composition of aerosol particles also determine their ability to nucleate clouds, hence affecting the regional weather and climate indirectly. Also, the composition of aerosols define the size of droplets formed in clouds through nucleation [Breon et al., 2002]. This variation in size of droplets affects the cloud reflectivity hence affect the climate by varying the reflection of solar radiation [Twomey, 1991].

The cloud droplet size distribution also affects the life-time of the cloud [Albrecht, 1981], and the life-time of the clouds not only impacts the regional weather, but also the climate, because if clouds live longer or not so long, this impacts the radiative budget as well. These are some of the indirect effects of aerosols on climate.

Even though these small particles have a big impact on environment, a fair share of the physical and chemical processes of aerosols is still not fully understood. Numerical models are important tools to assess the aerosol impact on climate [Ackermann et al., 1998, Gong et al., 2003, Pope and Howard, 1997, Whitby and McMurry, 1997, Zaveri et al., 2008]. It is a challenging task to represent aerosol processes in a global-scale model because the global models use grid sizes of about 100 km and aerosol processes occur at a micrometer length scales. This is why we need improved numerical models to better model the aerosol physics and its effects.

1.2 Numerical modeling of Aerosols

As discussed in the previous section, aerosol numerical modeling is important because the aerosols have significant impact on the Earth's energy budget and human health. There are three modeling approaches used in atmospheric sciences community, (1) modal approach, (2) sectional approach and (3) particle-resolved approach. As shown in Figure 1.3, each method quanti-

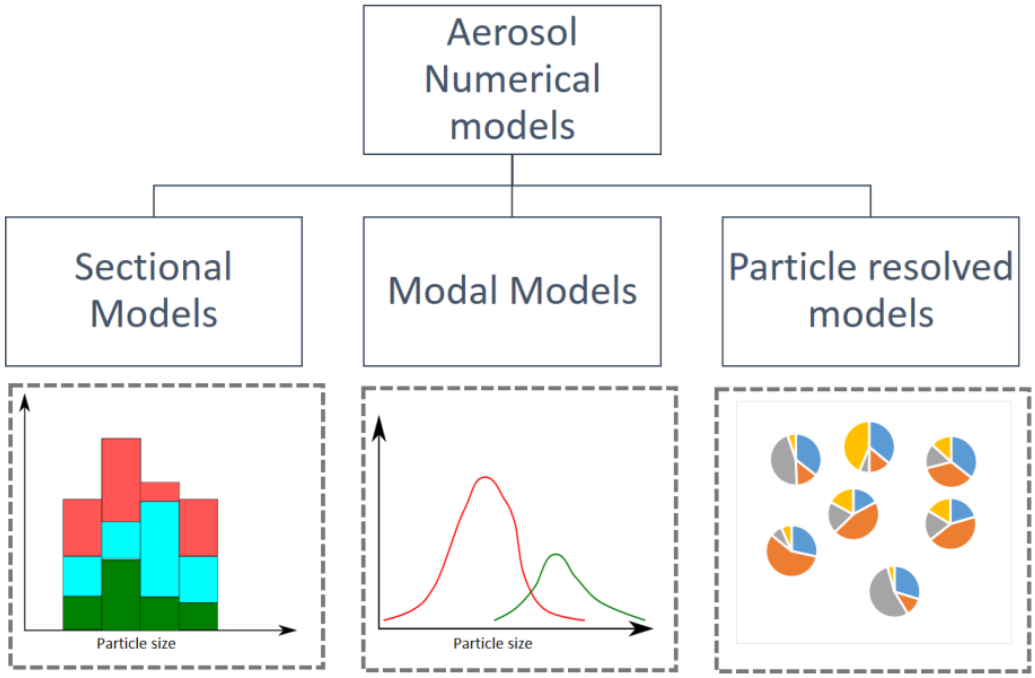

Figure 1.3: Aerosol numerical models classification.

fies particle size distribution in different ways. All numerical models usually assume that the aerosol particles are spherical in shape.

The Modal Aerosol Dynamics (MAD) approach represents the aerosol population by superposition of a finite number of particle size distributions called modes and all physical processes are modeled within these modes. As described in Whitby and McMurry [1997], the Moment Dynamics Equations are solved for zeroth, third and sixth moment of particle size to find the particle size distribution evolution with time, in a well-mixed box. The zeroth and the third moment signify the number concentration and the volume concentration of aerosol particles, respectively, while the sixth moment is proportional to the so called radar reflectivity. The total size distribution is considered as a superposition of multiple modes (log-normal distribution in Whitby and McMurry [1997]) which can interact with each other. This method is computationally less expensive as compared to others, but it makes some assumptions in keeping track of the composition of individual aerosol particles. One such assumption is that all the particles within each mode with this method are assumed to have a specific composition. This is a significant assumption since the aerosol particles, even of the same mode, are known

to vary drastically in composition. The MAD modeling approach is used in various global models (e.g. Bauer et al. [2008] and Stier et al. [2012]).

Another approach for modeling aerosols is Sectional modeling. Sectional models discretize the variable space into sections and store the number distribution or mass distribution in each section. A popular tool in the atmospheric sciences community to model aerosols is the community model of WRF-Chem (Weather Reasearch and Forecasting) [Grell et al., 2005, Peckham et al., 2012], which is used by many researchers for modeling the spatial and temporal evolution of gas and aerosol phase pollutants on a regional scale. The aerosol module of WRF-Chem can be used with size-resolved composition sectional model where all the particles of the same section are assumed to have identical composition. A comparative study was presented in Zhang et al. [1999] comparing modal approach with sectional approach to model aerosol dynamics. The study concluded that discretized sectional approach can produce major characteristics of particle size evolution. Sectional size resolved model has been implemented in various studies for aerosol dynamics [Meng et al., 1998, Wexler et al., 1994]. While assuming that each section contains particles with same composition can be a good approximation to estimate average aerosol compositions in a region, this assumption with aging processes can lead to particles which are different in size and composition as compared to the actual physical scenario.

A suitable model framework to track the detailed composition of aerosol population is particle-resolved models. For example, the particle-resolved aerosol model Part MC [Riemer et al., 2009, 2010, Zaveri et al., 2010] tracks the processes of coagulation, condensation, emission and dilution for a well-mixed box. Particle resolved methods have also been implemented in other works such as, Jaruga et al. [2013] and Shima et al. [2009]. Shima et al. [2009] implemented the particle resolved approach for cloud precipitation.

Aerosol particles in Part MC are treated individually so that their individual composition can be tracked during a simulation. The processes of transport and coagulation are modeled stochastically in Part-MC. Although computationally expensive, this model includes fewer assumptions as compared to aforementioned models and is more efficient in keeping track of composition of aerosols. While it started out as a box model, Part-MC has been recently extended to include stochastic methods for particle transport. The current numerical methods for particle transport in Part-MC, as described

in Curtis et al. [2016a,b], are very simple and of lower order in time and space. The goal of this thesis is the development of higher-order particle-resolved transport model and its validity with respect to the conventional finite volume scalar transport models.

1.3 Particle-resolved models: Part MC

Particle-resolved methods were introduced in Gillespie [1975], where the coagulation process in clouds was modeled stochastically. Later a more general stochastic simulation algorithm was derived in Gillespie [1977]. In Shima et al. [2009], particle/droplet positions were tracked with the particle resolved model of droplet condensation.

The particle-resolved model in Part MC uses a vector of dimension d to describe an aerosol particle. As described in Riemer et al. [2009], the vector consists of the mass of each of d species in a corresponding aerosol particle. Each vector μ represents a point or a position in a d dimensional composition space with the mass of each species as its components, $\mu_1, \mu_2 ..., \mu_{d-1}, \mu_d$. These particle composition vectors are added or subtracted for coagulation and condensation, gains and losses in a simulation. As mentioned in Riemer et al. [2009], the governing equation for particle evolution is given by,

$$\begin{aligned}\frac{\partial n(x,\mu,t)}{\partial t} = & \underbrace{\nabla \cdot [D_0 \cdot \nabla(n(x,\mu,t))]}_{\text{Turbulent diffusion}} - \underbrace{\nabla \cdot [u(x,t) n(x,\mu,t)]}_{\text{Advection}} \\ & + \underbrace{\frac{1}{2} \int_0^{\mu_1} .. \int_0^{\mu_d} K(\mu', \mu - \mu') n(x,\mu',t) n(x,\mu-\mu',t) d\mu_1 .. d\mu_d}_{\text{coagulation gain}} \\ & + \underbrace{\int_0^{\mu_1} .. \int_0^{\mu_d} K(\mu,\mu') n(x,\mu',t) n(x,\mu,t) d\mu_1 .. d\mu_d}_{\text{coagulation loss}} + \underbrace{\dot{n}_{\text{emission}}(x,\mu,t)}_{\text{emmisions}} \\ & - \underbrace{\sum_{l=1}^{C} \frac{\partial}{\partial \mu_l}(c_l I_l n(x,\mu,t))}_{\text{gas-particle transfer}} - \underbrace{\frac{\partial}{\partial \mu_{C+1}}(c_w I_w n(x,\mu,t))}_{\text{water transfer}} . \end{aligned} \tag{1.1}$$

where, $n(x,\mu,t)$ represents the particle size distribution at position x, at time t. D_0 is diffusion coefficient in air, K represents the coagulation kernel (i.e. probability function for particles μ and μ' to coagulate) and c_l represents the

mass of a gas specie. Transport (advection and diffusion) and coagulation gains and losses are modeled stochastically in Part-MC. The gas phase chemistry is modeled in chemistry modules using MOSAIC [Zaveri et al., 2008]. This thesis only focuses on the numerical modeling of first two terms of the RHS of equation (1.1), i.e. the transport terms.

1.4 Contribution of thesis: Stochastic particle-resolved transport

Since each particle is represented by a distinct vector for a given time step, it is to be treated distinctly, even for transport. Since keeping track of positions of individual particles is computationally very expensive, a grid-based stochastic method may be a more practical trade-off between desired accuracy and computational expense. In this work, a model is proposed for the transport of particles using a stochastic multinomial sampling algorithm based on the already existing finite volume methods for passive scalar transport.

Among other studies for particle transport, a numerical study for a reactive-diffusive system has been carried out on a finite volume grid in Lampoudi et al. [2009]. Lampoudi et al. [2009] developed transport with Multinomial Simulation Algorithm (MSA) which uses operator splitting for stochastic diffusion and stochastic reaction simulations. This algorithm is particle resolved, but only addresses the part of the problem that pertains to vertical diffusion. In this thesis work, horizontal advection has also been addressed by defining a more general transport formulation.

A stochastic particle-resolved advection-diffusion model was described in Jain [2011]. The Particle grid method (PGM), in Jain [2011] laid the basic mathematical theory for transport and described its consistency and convergence. This thesis, however, models the stochastic transport in a flux based framework which can be included easily in WRF transport module. The current work also illustrates the approach for applying the proposed method for higher-order transport schemes, which will be discussed in Chapter 3.

In a horizontal plane for an atmospheric scenario, the transport is dominated by advection and vertical transport is dominated by turbulent diffusion. In this work, we address advection and diffusion of particles separately

and discuss their theoretical and numerical convergence.

1.5 Thesis Structure

This research work is based on exploring higher order methods for stochastic transport in a grid-based system. Although this work does not include chemical and physical reactions (coagulation, condensation and source emissions) among aerosols, each particle is distinctly resolved for the study. The aim of this work is to formulate and implement stochastic advection and diffusion, and quantify the corresponding errors. The formulation starts with introduction of passive scalar transport and will lead to flux-based particle transport in Chapter 2. Chapter 3 will discuss explicit numerical schemes for advection and diffusion. Chapter 4 presents the error analysis and grid-convergence study for all the numerical explicit schemes discussed in Chapter 3 and 2. Numerical results of test cases with the description of boundary conditions and initial conditions will be listed in Chapter 5. Conclusions from the results and further work are discussed in Chapter 6 of this document.

CHAPTER 2

PARTICLE TRANSPORT IN 1-DIMENSIONAL GRID

In this chapter, starting with an introduction to one-particle transport, finite-volume method for transport of a passive scalar and a stochastic flux-based particle transport method for multiple particles will be discussed. Also, the consistency of stochastic method will be theoretically proved at the end of this chapter.

2.1 Transport of a particle : Fokker-Planck Equation

Movement of a free particle due to the process of diffusion has been described as Brownian motion. The mathematical description of Brownian motion of suspended particles in a solvent was originally presented in Einstein [1905] and was later described in different forms by several authors [Furth and Cowper, 1956]. If a single particle is considered for transport in a 1D space with a given velocity field, its motion can be formulated by Smoluchowski equation

$$dx(t) = u(x,t)dt + \sigma(x,t)dW(t). \tag{2.1}$$

Here, position $x(t)$ is a random variable, u is the velocity of particle, t is the time, dW is the brownian motion term or Wiener's process [Higham, 2001, Titulaer, 1978] which scales as $[\sqrt{dt}\ \mathrm{N}(0,1)]$ with time, and σ is defined as the deviation of the linear movement of the particle in time dt. The relationship between the random variable $x(t)$ and the probability density function for the particle $p(x,t)$ is given by Fokker-Planck equation

$$\frac{\partial p(x,t)}{\partial t} = -\frac{\partial (u(x,t)p(x,t))}{\partial x} + \frac{\partial^2 (D(x,t)p(x,t))}{\partial x^2}, \tag{2.2}$$

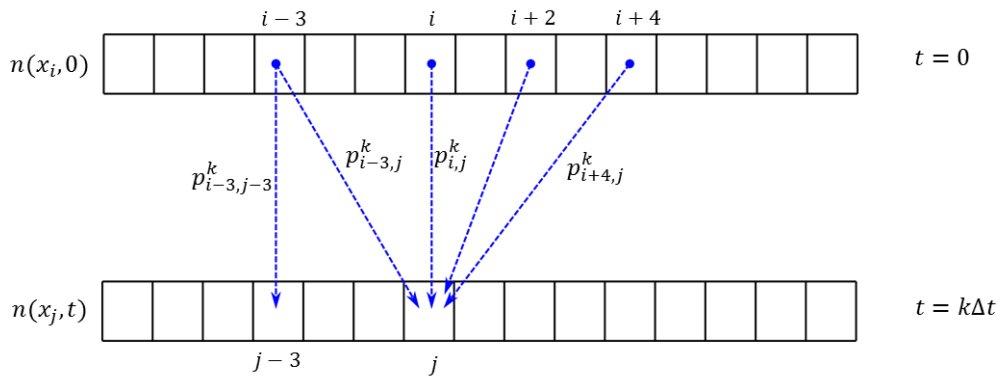

Figure 2.1: Probability for particle transport for time $t = k\triangle t$. Particle population in a grid-cell depends on the particles in other grid-cells in previous time-steps

where, $D = \sigma^2/2$, is the diffusion coefficient. Since the initial location of the particle is known, $p(x, t = 0)$ is a Dirac-delta function centered at the given location. Equation (2.2) can be solved as an initial value problem to find the spatial probability distribution for the particle in future time.

Since the equation (2.2) is solved by numerical methods, the space can be discretized into number of finite-volume grid-cells as shown in Figure 2.1. If more than one number of particles is initially placed in a same grid-cell, the probability distribution for each particle is given by the numerical solution of equation (2.2). Since interactions between particles are ignored, each particle movement simulated separately can be superimposed to produce results for a system consisting of many particles. For particles present in the same grid-cell at $t = 0$, a difference in their location/grid-cell, $x_i(t)$, in future times is introduced by stochastic components of the simulation.

The probabilities p_{ij} are calculated by solving equation (2.2) in each cell with initial conditions defined in all n_{x} cells. For example, a grid with initial conditions and probabilities of particles to commute from an initial distribution are given in Figure 2.1. Considering an initial spatial distribution of particle number as $n(x_i, t = 0)$ in a one-dimensional grid with grid-cell number denoted by index i, the particle number distribution in future times

can be found by sampling the initial distribution with probabilities,

$$\begin{aligned} p_{ij}^k = &\text{ Probability of particle in cell } i \text{ to move to cell } j \text{ at time-step } k, \\ t = k\triangle t, &\triangle t \text{ is the time-spacing,} \\ n(x_j, t) \sim \sum_{i=1}^{n_\mathrm{x}} &\text{multinomial}(n(x_i, 0), p_{ij}^k). \end{aligned} \tag{2.3}$$

The above method could have been a good reduction in computational power since it only requires initial conditions and probabilities to find a distribution at any desired time-step. But because of the other phenomena such as coagulation and condensation are to be implemented at each time-step, the spatial distribution of particles is required at each time-step.

The number of events for multinomial sampling depends on the number of grid cells. For a grid with n_x grid cells, this method require sampling on about n_x^2 probabilities. An increase in the grid resolution causes problem in sampling as the probability associated with each grid keeps reducing with grid-spacing and computational power required increases drastically. But if we limit the movement of a particle to one grid-cell per time-step, the problem can be shaped as flux-based finite volume form. In this work, instead of defining n_x exhaustive events for a one-dimensional grid, the method is flux based, has two exhaustive events for a particle in a grid-cell and is compatible with finite volume space discretization. More about this will be described in Section 2.3.

2.2 Passive Scalar Transport (PST)

Aerosol particles have a very low mass [Jacobson Chapter 5, 2012] of the order of 10 fg, and their momentum change does not change the velocity field significantly. This makes aerosol particle bulk-transport similar to transport of a passive-scalar in a velocity field. Scalar transport consists of (1) advection (2) and diffusion phenomena. The scalar transport is given by the following partial differential equation,

$$\frac{\partial q}{\partial t} = -\nabla \cdot (uq) + (\nabla \cdot D_0(\nabla q)) + R, \tag{2.4}$$

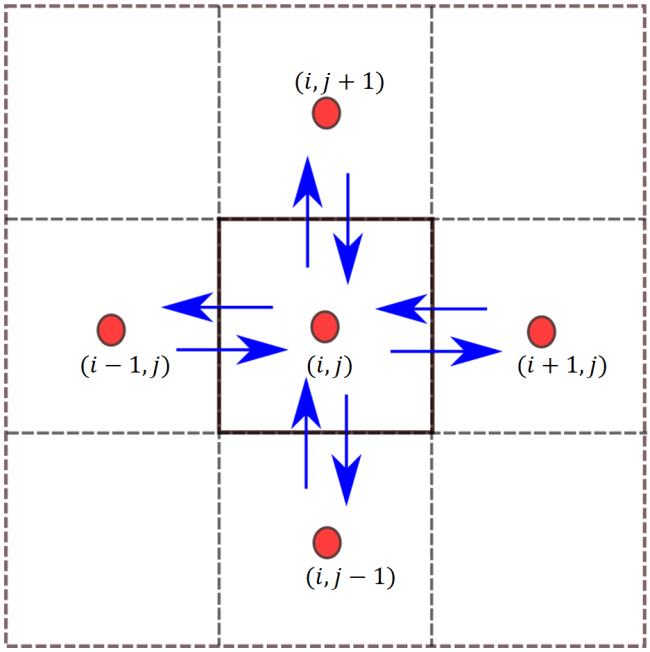

Figure 2.2: Fluxes for a two-dimensional finite volume grid. Net flux is the difference in influx and outflux from a face(indicated by blue arrows).

where the terms, $-\nabla \cdot (uq)$,$(\nabla \cdot D_0(\nabla q))$ and R are advection, diffusion and reaction parts of the scalar transport equation respectively. The variable q is the exact passive scalar for transport. This equation can be solved by numerous numerical methods. Finite volume methods are one of the most popular methods for computational fluid dynamics used in commercial [ANSYS, CD-adapco, 2009] and open-source models [Jasak, 2009]. For a finite volume grid, this equation can be written in forward single time-step flux-based form as given as,

$$Q_i^{k+1} = Q_i^k + \left(\sum_{s=1}^{S} (F_s^k)_i \right). \tag{2.5}$$

Here the term, S is number of faces in cell i and Q is the finite-volume discretized value (i.e. it's average value for a grid-cell) of passive scalar as shown in Figure 2.2. Flux through s^{th} face of grid cell i is represented by $(F_s^k)_i$. More description to this is provided in Appendix A.

Equation (2.4) can be represented in a one-dimensional form for finite

volume grid in Figure 2.3, and its corresponding PDE is given by

$$\frac{\partial q}{\partial t} = -\frac{\partial (uq)}{\partial x} + \frac{\partial}{\partial x}\left[D_0 \frac{\partial (q)}{\partial x}\right]. \tag{2.6}$$

A structured 1D finite-volume grid has two faces for each grid-cell as shown in Figure 2.3. The flux-based explicit formulation for equation (2.6) is given by,

$$Q_i^{k+1} = Q_i^k - \left(F_{i+1/2}^k - F_{i-1/2}^k\right)_{\mathrm{FV}}. \tag{2.7}$$

The subscript $i + 1/2$ and $i - 1/2$ represent the right and the left faces of grid-cell i respectively, in a one-dimensional grid as shown in Figure 2.3. The flux F takes different forms as a function of average cell values Q_i^k, Q_{i-1}^k, Q_{i+1}^k etc. depending on the stencil used for space discretization. As an example, for an expression for flux we can write,

$$(F_{i+1/2}^k) = c_0 Q_i^k + c_{-1} Q_{i-1}^k + c_{+1} Q_{i+1}^k. \tag{2.8}$$

For this equation it is assumed that flux depends on average scalar values of grid-cells i, $i-1$ and $i+1$ with coefficients c_0, c_{-1} and c_{+1} respectively. The flux vector for $n_{\mathrm{x}}+1$ faces in one-dimensional formulation can be represented as product of a coefficient matrix and a vector containing values of scalar Q in the space.

$$\mathbf{F}^k = C\mathbf{Q}^k \tag{2.9}$$

$$C = C_{\mathrm{adv}} + C_{\mathrm{diff}}. \tag{2.10}$$

The sparse coefficient matrix is given by,

$$C = \begin{bmatrix} \dots & & \text{Boundary} & \text{Cond} & \dots & \\ \vdots & \ddots & & \dots & \vdots & 0 \\ 0 \dots & c_{-1} & c_0 & c_{+1} & \dots & 0 \\ \dots & 0 & c_{-1} & c_0 & c_{+1} \dots & \\ \dots & & & \ddots & \vdots & 0 \\ \dots & & \text{Boundary} & \text{Cond} & \dots & \end{bmatrix}$$

The coefficient matrix can be split into advection (C_{adv}) and diffusion

(C_{diff}) parts representing fluxes corresponding to respective phenomena. More about different forms of coefficient matrix C will be described in chapter 3.

2.3 Flux-based particle transport (FBPT)

The flux-based particle transport (FBPT) method is similar to the passive scalar transport (PST) as described in equations (2.5) and (2.7). It also involves flux terms through grid-faces similar to equation (2.5) but we consider fluxes of discrete particles rather than fluxes of scalar quantities. Since this work is based on resolving individual particles, rather than using the net flux through a grid-face which is common in PST, the flux movement in both directions (in and out) of faces has to be considered as shown in Figure 2.3.

If all particles are considered identical, then a finite-volume formulation in a flux-based form for number of particles, N_i^k, is given by equation,

$$N_i^{k+1} = N_i^k - \left(G_{i+1/2}^k - G_{i-1/2}^k\right). \tag{2.11}$$

Here, $G_{i+1/2}^k$ and $G_{i-1/2}^k$ represent the total flux for number of particles through the faces of grid-cell i. Since we resolve individual particles, these fluxes have to be calculated stochastically considering the probability of each particle to commute between neighboring grid-cells. For each aerosol particle, there is a probability for its movement to neighboring grid-cell or to stay in the same cell, which depends on the flow velocity field, the grid size, the spatial distribution of particle number and the time-step. Since the only attribute considered in this model is the number of particles, the probability described above is equal for all the particles present in a grid-cell.

The probability can be determined analogously to that of scalar advection flux expressions, and then normalizing it with the total number of particles present in the grid-cell gives the desired expression of probability. As discussed earlier, there will be an influx as well as outflux of distinct particles from all the grid-faces of a grid cell as shown in Figure 2.3. If only one-dimensional transport is considered each grid-cell will only contain East (E) and West (W) grid-faces and there will be four flux terms for the two faces of a cell as shown in Figure 2.3. For defining a probability model, there are three exhaustive events to be considered, the particle movement through (1)

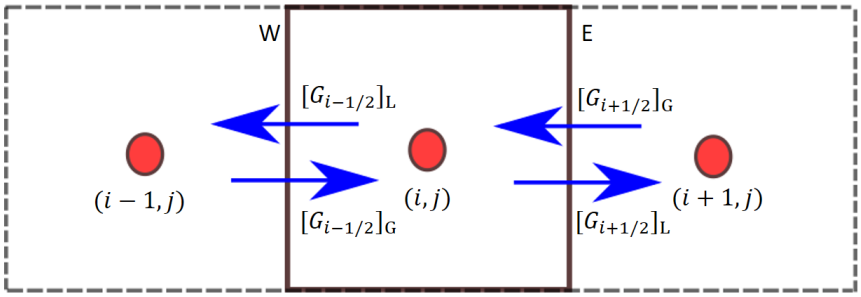

Figure 2.3: One dimensional grid for flux-based particle transport (FBPT). Subscripts L and G means loss and gain flux of particles from the grid-cell (i, j) through the grid-faces, respectively. Notations W and E denote the grid-faces $i - 1/2$ and $i + 1/2$ respectively.

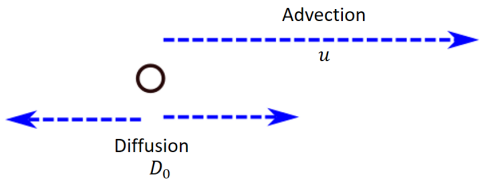

Figure 2.4: Advection and diffusion processes for a particle. Net transport of a particle is given by the superposition of both processes.

the right face (p_{R}) and (2) the left face (p_{L}), or (3) staying in same grid-cell. Since these events are exhaustive, only two of them, are independent. The probabilities p_{R} and p_{L} depend on the processes of advection and diffusion. Also, for valid probabilities, $N_i^k \neq 0$. Since the algorithm performs Bernoulli's trials (described in next subsection), if $N_i^k = 0$ occurs, the algorithm will automatically skip the grid cell while evaluating fluxes across the faces. As discussed in the previous section, since linearity in the processes of diffusion and advection are considered for this work, these processes can be discussed separately and then superposition can be used to model transport phenomena as shown in Figure 2.4. In the following sections, the advection and diffusion processes are discussed individually.

2.3.1 Particle advection

The process of advection takes place under the influence of a velocity field. This makes advection unidirectional, and the direction of its influence is the same as the direction of velocity at that point in space. Hence, the probability values for particles in i^{th} grid-cell to move to a neighboring grid-cell can be defined by $(P_{\mathrm{adv}}^k)_i$. Probability values P_{adv}^k can be determined as,

$$[(P_{\mathrm{adv}}^k)_i]_{+\mathrm{x}} = \begin{cases} \left[\left(\frac{1}{N_i^k}\right)\right] |\{C_{\mathrm{adv}}\mathbf{N}^k\}_i| & u_{i+1/2} \geq 0 \\ 0 & u_{i+1/2} < 0, \end{cases} \tag{2.12}$$

$$[(P_{\mathrm{adv}}^k)_{i+1}]_{-\mathrm{x}} = \begin{cases} 0 & u_{i+1/2} \geq 0 \\ \left[\left(\frac{1}{N_{i+1}^k}\right)\right] |\{C_{\mathrm{adv}}\mathbf{N}^k\}_{i+1}| & u_{i+1/2} < 0. \end{cases} \tag{2.13}$$

The terms $[(P_{\mathrm{adv}}^k)_i]_{+\mathrm{x}}$ and $[(P_{\mathrm{adv}}^k)_i]_{-\mathrm{x}}$ are the probabilities of a particle in grid-cell i to move in +x direction (right) and -x direction (left) respectively. The number of particles in each grid cell and the applied boundary conditions are represented by vector $\mathbf{N}^k$. The values found in the equations (2.12) and (2.13) represent the probability of particles in cells (i) and $(i+1)$, adjacent to the face $(i+1/2)$, to move through the face in the direction determined by the sign of the velocity value (i.e. direction) at the face. The flux vector $\mathbf{G}^k$ is calculated by performing independent Bernoulli trials on the particles

present in a grid-cell with probability P_i^k. If only advection is considered for transport (i.e. diffusion is absent), the flux in the form of a number of discrete particles can be defined as,

$$\{[(G^k_{\text{diff}})_{i-1/2}]_{\text{L}}, [(G^k_{\text{diff}})_{i+1/2}]_{\text{L}}\} \sim \text{multinomial}(N_i^k, [(P_{\text{adv}})_i]_{-\text{x}}, [(P_{\text{adv}})_i]_{+\text{x}}). \tag{2.14}$$

The order of grid-convergence and accuracy depends on the coefficient matrix C_{adv} which defines the type of advection scheme used in the problem. More about this will be discussed in Chapter 3. Results for 1D advection tests with their convergence will be discussed in Chapter 5.

2.3.2 Particle diffusion

The process of diffusion, unlike advection, is not unidirectional. Only parameter associated with the diffusion is the diffusion coefficient, D_0, which defines the time-scale of the random diffusion process. Analogous to the treatment in particle advection, the particle-resolved diffusion process treats individual particles distinctly and hence, the net-flux theory which is used in scalar FV transport (PST) cannot be used here. Instead, the particles should have the possibility of commuting in any direction irrespective of the net-flux direction. In this work, the flux based transport methods are developed which are derived and manipulated from scalar transport methods, and use the same coefficient matrix as scalar transport methods (PST). As established in Appendix A, the diffusion flux of a passive scalar depends on the gradient of scalar in space.

Here we are dealing with movement of particles irrespective of gradient direction, and hence the problem should be split into multiple parts. As an example, if the finite-volume grid is split off a face shown in Figure 2.5, there will be particles moving from side (1) to (2) and vice-versa, making the net particle population flux being difference between the two. For defining two fluxes separately, the coefficient matrix for diffusion, C_{diff}, can be split into two parts, (1) $C_{\text{diff}+\text{x}}$ and (2) $C_{\text{diff}-\text{x}}$, where they represent the coefficient matrices for sides (1) and (2), respectively. Hence, the diffusion flux for

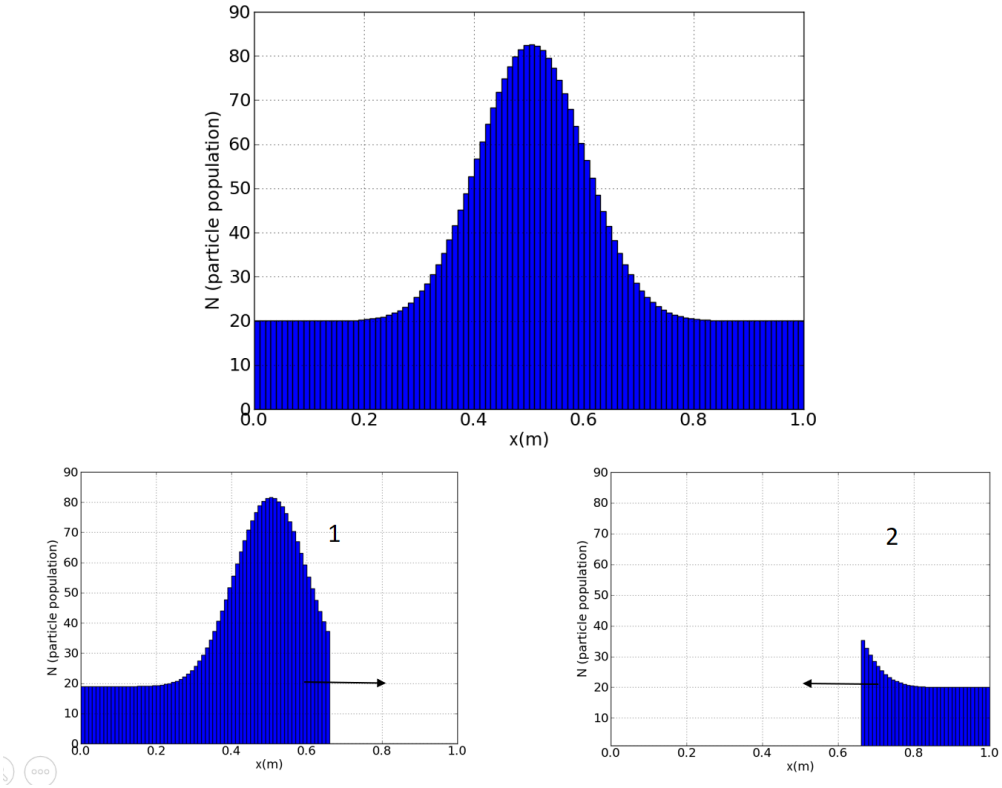

Figure 2.5: A schematic for diffusion process. The top figure shows a particle population distribution at some time-step. The distribution when split into two from a face, the two sides (1 & 2) look like as shown in bottom figures. The particles can move from side 1 to 2 and vice-versa as indicated in the figure.

scalar transport can be written as

$$(F^k_{\text{diff}})_{i+1/2} = \underbrace{(d_0 Q^k_i + d_{-1} Q^k_{i-1})}_{\text{side 1}} + \underbrace{d_{+1} Q^k_{i+1} + d_{+2} Q^k_{i+2}}_{\text{side 2}}.$$

The terms d_{-1}, d_{+1}, d_{-2} and d_{+2} represent the coefficients for the grid-cell average values for neighboring grid-cells of cell i. In matrix form, above equation can be written as,

$$\mathbf{F}^k_{\text{diff}} = C_{\text{diff}} \mathbf{Q}^k, \tag{2.15}$$

$$C_{\text{diff}} = C_{\text{diff}\,+\text{x}} + C_{\text{diff}\,-\text{x}}. \tag{2.16}$$

Now that we have addressed the particle transfer from both sides of a face, the probability for movement of each particle in neighboring grid-cells will be found next. Each particle will have probabilities, $[(P_{\text{diff}})^k_i]_{+\text{x}}$ and $[(P_{\text{diff}})^k_i]_{+\text{x}}$, to go to either direction of the grid-cell. Here, the probability of a particle in a grid-cell i, moving to left or right due to the diffusion process has been labeled as $(P_{\text{diff}})_i$,

$$[(P_{\text{diff}})^k_i]_{+\text{x}} = \left| \left[\left(\frac{1}{N^k_i} \right) \right] \{ C_{\text{diff}\,+\text{x}} \mathbf{N}^k \}_i \right|, \tag{2.17}$$

$$[(P_{\text{diff}})^k_{i+1}]_{-\text{x}} = \left| \left[\left(\frac{1}{N^k_{i+1}} \right) \right] \{ C_{\text{diff}\,-\text{x}} \mathbf{N}^k \}_i \right|. \tag{2.18}$$

As illustrated in Figure 2.3, there will be four flux terms for a 1D diffusion, namely loss and gain terms from both faces. The loss flux for diffusion can be described as,

$$\{[(G^k_{\text{diff}})_{i-1/2}]_{\text{L}}, [(G^k_{\text{diff}})_{i+1/2}]_{\text{L}}\} \sim \text{multinomial}(N^k_i, [(P_{\text{diff}})^k_i]_{-\text{x}}, [(P_{\text{diff}})^k_i]_{+\text{x}}). \tag{2.19}$$

For a uniform grid, the loss flux term from grid-cell $i+1$ becomes the gain flux ($[G_{\text{E}}]_{\text{G}}$) for grid-cell i, and the loss from grid-cell $i-1$ also becomes the gain flux for grid-cell i. Hence, equation (2.19) defines all the diffusion flux terms for the problem.

The necessity of splitting the diffusion coefficient matrix can be observed for a test case with no spatial gradient for particle concentration. For a finite-volume PST, we would expect that the distribution does not change with

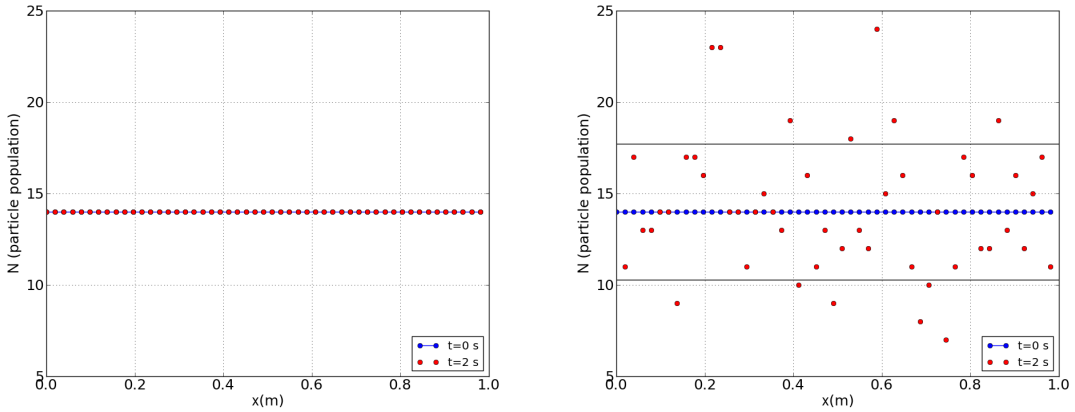

(a) Without splitting coefficent matrix

(b) With splitting coefficent matrix

Figure 2.6: Effect of splitting C_{diff}. Particles can be transported and mixed even in the absence of particle concentration gradient. This is necessary when all the particles are distinct.

time. But when particles are present, random mixing should occur and the domain should eventually reach a steady state. As seen in Figure 2.6, mixing of particles, as time progresses, can be observed using the split diffusion coefficient matrix. More details on this test will be discussed in Section 5.2.

Now that advection and diffusion processes have been discussed individually, in next sub-section, both processes will be combined using superposition for modeling the transport of particles.

2.3.3 Particle advection and diffusion

As discussed previously and shown in Figure 2.3 and 2.4, each particle in a grid-cell will have a probability to move to left or right grid-cell, or to stay in the same grid-cell during the next time-step. Since the probabilities are based on flux across the faces, they can be added when superimposed to find the net probability of a particle to commute. Using superposition of advection and diffusion processes, probabilities of a particle can be defined as,

$$[(P)_i^k]_{+\text{x}} = [(P_{\text{diff}})_i^k]_{+\text{x}} + [(P_{\text{adv}})_i^k]_{+\text{x}}, \tag{2.20}$$

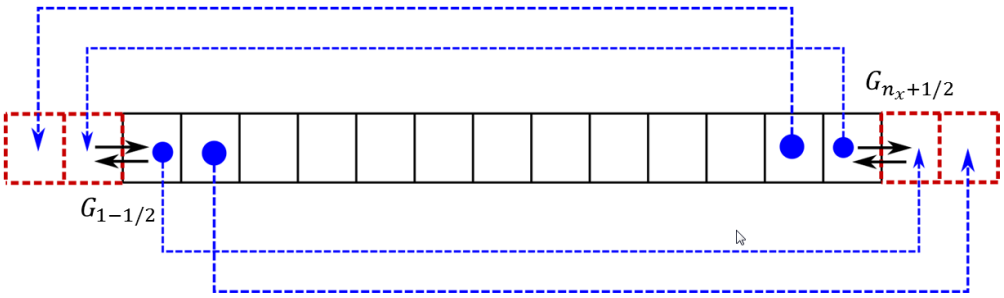

Figure 2.7: Periodic boundary conditions applied on a 1D grid. The cell in red represent the ghost boundary cells whose cell average values are assigned according to the type of boundary to be imposed.

$$[(P)_i^k]_{-\mathrm{x}} = [(P_{\mathrm{diff}})_i^k]_{-\mathrm{x}} + [(P_{\mathrm{adv}})_i^k]_{-\mathrm{x}}. \tag{2.21}$$

The terms $[(P)_i^k]_{+\mathrm{x}}$ and $[(P)_i^k]_{-\mathrm{x}}$ represent the probabilities of a particle in grid-cell i to move in +x or -x direction grid-cell respectively.

Here, advection affects the particle transport only in the direction of flow whereas diffusion effects are not unidirectional. Similar to the loss flux in diffusion, the flux terms for advection-diffusion system can be described as,

$$\{[(G^k)_{i-1/2}]_{\mathrm{L}}, [(G^k)_{i+1/2}]_{\mathrm{L}}\} \sim \mathrm{multinomial}(N_i^k, [(P)_i^k]_{-\mathrm{x}}, [(P)_i^k]_{+\mathrm{x}}). \tag{2.22}$$

Also, similar to previous sub-section, the loss terms in equation (2.22) completely represents the particle transport.

2.3.4 Boundary conditions

The boundary conditions for passive scalar transport, PST, are formulated in the form of average scalar values in each grid-cell, and the flux values calculated implicitly have the assigned boundary conditions in them. For imposing the boundary conditions, fictitious grid-cells are put at the boundaries, and they are called ghost cells. Assigning values to these ghost cells is sufficient for imposing a boundary for PST. For example, if periodic boundary is to be assigned for PST, the ghost cells will have values from the cells adjacent to the other boundary as shown in Figure 2.7. With this boundary

in place, the flux boundary condition for PST,

$$F_{n_x+1/2} = F_{1-1/2},$$

is not necessary as the assumed ghost cell values will take care of this boundary condition. However, for FBPT, the flux values calculated are stochastic in nature which requires assigning some specific flux value at the boundaries which will not depend on the stochastic nature of formulation. Continuing the example given above, to conserve the number of particles in the domain, flux boundary conditions of,

$$[G_{n_x+1/2}]_{\mathrm{L}} = [G_{1-1/2}]_{\mathrm{G}},$$
$$[G_{n_x+1/2}]_{\mathrm{G}} = [G_{1-1/2}]_{\mathrm{L}},$$

have to be imposed along with the assignment of particle population/number values for the ghost cells for the calculations of probabilities. Similarly, for a wall boundary condition, the flux values on boundary have to be explicitly specified (equal to zero) in addition to satisfying zero gradient in particle population/number values at the boundary.

In the next section, consistency of FBPT will be discussed with respect to finite-volume solution of PST.

2.4 Consistency of FBPT

The discussion in the previous section deals with the individual particles being transported in one dimension. Since the formulation of stochastic method was derived from finite-volume passive scalar transport, FV-PST, the numerical solution of FBPT should converge to the PST solution when the number of particles is large enough to behave like a continuous scalar field. We will be dealing with particle concentration for this section along with the absolute number of particles in a grid-cell. We define a term sample volume, V to represent the volume (m^3) to define the particle concentration of aerosols,

$$Q_{\mathrm{part}_i}{}^k = \frac{N_i^k}{V}. \tag{2.23}$$

The sampling volume, V, in this work is defined as a constant so that the initial particle concentration (Q^0_{part}) is exactly the same as the initial passive scalar concentration (Q^0) with different total number of particles (N), so that the FBPT results can be compared with the FV-PST results.

Theorem 1. *If the initial particle population distribution is defined as,*

$$N_i^0 = VQ_i^0,$$

and the flux through faces is defined as,

$$\begin{aligned}\{[(G^k)_{i-1/2}]_{\text{L}}, [(G^k)_{i+1/2}]_{\text{L}}\} &\sim \text{multinomial}(N_i^k, [(P)_i^k]_{-\text{x}}, [(P)_i^k]_{+\text{x}}),\\ N_i^{k+1} &= N_i^k - \left([(G^k)_{i+1/2}]_{\text{L}} + [(G^k)_{i+1/2}]_{\text{L}}\right)\\ &\quad + \left([(G^k)_{i-1/2}]_{\text{G}} - [(G^k)_{i+1/2}]_{\text{G}}\right),\end{aligned}$$

then the expected value of FBPT is given by,

$$\text{E}[N_i^k] = (VQ_i^k). \tag{2.24}$$

Proof. It is given that the theorem statement is true for $k = 0$. Now, let's assume that the theorem statement is true for all i's at time step k,

$$\text{E}[N_i^k] = VQ_i^k. \tag{2.25}$$

Given above conditions and assumptions, if the theorem statement is also true for time step $k + 1$, then by the principle of Mathematical Induction, Theorem 1 is true for all time steps.

Since the mean value of multinomial distribution multinomial$\{w, r_1, r_2, ..., r_n\}$ is given by $\{wr_1, wr_2, ..., wr_n\}$, the mean value of fluxes is,

$$\begin{aligned}\text{E}([(G^k)_{i-1/2}]_{\text{L}}|\mathbf{N^k}) &= N_i^k[(P)_i^k]_{-\text{x}},\\ \text{E}([(G^k)_{i+1/2}]_{\text{L}}|\mathbf{N^k}) &= N_i^k[(P)_i^k]_{+\text{x}},\\ \text{E}([(G^k)_{i-1/2}]_{\text{G}}|\mathbf{N^k}) &= N_{i+1}^k[(P)_{i+1}^k]_{-\text{x}},\\ \text{E}([(G^k)_{i+1/2}]_{\text{G}}|\mathbf{N^k}) &= N_{i-1}^k[(P)_{i-1}^k]_{+\text{x}}.\end{aligned} \tag{2.26}$$

Now, the particle population for the next time step is given by,

$$\begin{aligned} N_i^{k+1} = N_i^k &- \left([(G^k)_{i+1/2}]_{\mathrm{L}} + [(G^k)_{i+1/2}]_{\mathrm{L}}\right) \\ &+ \left([(G^k)_{i-1/2}]_{\mathrm{G}} - [(G^k)_{i+1/2}]_{\mathrm{G}}\right). \end{aligned}$$

Mean value of cell population is given by,

$$\begin{aligned} \mathrm{E}[N_i^{k+1}|\mathbf{N^k}] = \mathrm{E}[N_i^k|\mathbf{N^k}] &+ \left[\mathrm{E}([(G^k)_{i+1/2}]_{\mathrm{G}}|\mathbf{N^k}) - \mathrm{E}([(G^k)_{i+1/2}]_{\mathrm{L}}|\mathbf{N^k})\right] \\ &+ \left[\mathrm{E}([(G^k)_{i-1/2}]_{\mathrm{G}}|\mathbf{N^k}) - \mathrm{E}([(G^k)_{i-1/2}]_{\mathrm{L}}|\mathbf{N^k})\right] \end{aligned}$$

Substituting the mean values of fluxes from equation (2.26),

$$\begin{aligned} \mathrm{E}[N_i^{k+1}|\mathbf{N^k}] &= \mathrm{E}[N_i^k|\mathbf{N^k}] + \left[N_{i+1}^k[(P)_{i+1}^k]_{-\mathrm{x}} - N_i^k[(P)_i^k]_{-\mathrm{x}}\right] \\ &\quad + \left[N_{i-1}^k[(P)_{i-1}^k]_{+\mathrm{x}} - N_i^k[(P)_i^k]_{+\mathrm{x}}\right] \\ \mathrm{E}[N_i^{k+1}|\mathbf{N^k}] &= N_i^k + [(CN)_{i+1} - (CN)_i] \\ \mathrm{E}(\mathrm{E}[N_i^{k+1}|\mathbf{N^k}]) &= \mathrm{E}(N_i^k) + \left[\mathrm{E}(CN^k)_{i+1} - \mathrm{E}(CN^k)_i\right] \\ \mathrm{E}[N_i^{k+1}] &= VQ_i^k + V\left[(CQ^k)_{i+1} - (CQ^k)_i\right]. \end{aligned}$$

From the definition of finite volume flux in equation (2.9) of PST,

$$\begin{aligned} \mathrm{E}[N_i^{k+1}] &= V\left[Q_i^k + \left(F_{i-1/2}^k - F_{i+1/2}^k\right)\right] \\ \mathrm{E}[N_i^{k+1}] &= VQ_i^{k+1}. \end{aligned}$$

By the principle of Mathematical Induction, this proves that Theorem 1 holds true for all values of k with a constant value of V, sample volume.

□

Theorem 1 proves that if the FBPT is run for multiple times to collect statistical data, the mean value of particle concentration will be equal to PST, which was our initial hypothesis at the beginning of this section. This also means that,

$$\mathrm{E}[{Q_{\mathrm{part}}}_i^k] = Q_i^k. \tag{2.27}$$

Now that the expected value of particle concentration has been discussed, the convergence of FBPT to PST in the limit of total number of particles (i.e. V) going to infinity will be discussed.

Theorem 2. *If particle concentration is defined as ,*

$$
\begin{aligned}
{Q_{\text{part}}}_i^k &= \frac{N_i^k}{V} \\
N_i^0 &= V Q_i^0 \\
\{[(G^k)_{i-1/2}]_{\text{L}}, [(G^k)_{i+1/2}]_{\text{L}}\} &\sim \text{multinomial}(N_i^k, [(P)_i^k]_{-\text{x}}, [(P)_i^k]_{+\text{x}}), \\
N_i^{k+1} &= N_i^k - \left([(G^k)_{i+1/2}]_{\text{L}} + [(G^k)_{i-1/2}]_{\text{L}}\right) \\
&\quad + \left([(G^k)_{i-1/2}]_{\text{G}} + [(G^k)_{i+1/2}]_{\text{G}}\right),
\end{aligned}
$$

then,

$$
\lim_{V\to\infty} {Q_{\text{part}}}_i^k = Q_i^k. \tag{2.28}
$$

Proof. It is assumed that the statement is true for initial time $t = 0$,

$$
\lim_{V\to\infty} {Q_{\text{part}}}_i^0 = Q_i^0.
$$

Lets assume the statement,

$$
\lim_{V\to\infty} {Q_{\text{part}}}_i^k = Q_i^k
$$

is true for some k. From expressions for particle fluxes in equation (2.26),

$$
\begin{aligned}
\text{E}([(G^k)_{i-1/2}]_{\text{G}}) - \text{E}([(G^k)_{i-1/2}]_{\text{L}}) &= V F_{i-1/2}^k, \\
\text{E}([(G^k)_{i+1/2}]_{\text{L}}) - \text{E}([(G^k)_{i+1/2}]_{\text{G}}) &= V F_{i+1/2}^k.
\end{aligned}
$$

Since neither V or F^k are stochastic parameters,

$$
\begin{aligned}
\lim_{V\to\infty} \frac{1}{V} \left[\text{E}([(G^k)_{i-1/2}]_{\text{G}}) - \text{E}([(G^k)_{i-1/2}]_{\text{L}})\right] &= F_{i-1/2}^k, \\
\lim_{V\to\infty} \frac{1}{V} \left[\text{E}([(G^k)_{i+1/2}]_{\text{L}}) - \text{E}([(G^k)_{i+1/2}]_{\text{G}})\right] &= F_{i+1/2}^k.
\end{aligned} \tag{2.29}
$$

This proves that the mean value of stochastic flux converges to the PST finite-volume flux in the limit $V \to \infty$.

The variance of a multinomial distribution, multinomial$\{w, r_1, r_2, ..., r_n\}$, is given by is $\{wr_1(1-r_1), wr_2(1-r_2), ..., wr_n(1-r_n)\}$. The variance of the stochastic flux $([(G^k)_{i-1/2}]_{\text{L}})$ is given by,

$$\sigma^2\left[\frac{1}{V}([(G^k)_{i-1/2}]_{\mathrm{L}})\right] = \frac{1}{V^2}N_i^k[(P)_i^k]_{-\mathrm{x}}(1-[(P)_i^k]_{-\mathrm{x}}),$$
$$\lim_{V\to\infty}\left[\sigma^2\left[\frac{1}{V}([(G^k)_{i-1/2}]_{\mathrm{L}})\right]\right] = \lim_{V\to\infty}\frac{1}{V}{Q_{\mathrm{part}_i}}^k[(P)_i^k]_{-\mathrm{x}}(1-[(P)_i^k]_{-\mathrm{x}}),$$
$$\lim_{\mathrm{V}\to\infty}\left[\sigma^2\left[\frac{1}{V}([(G^k)_{i-1/2}]_{\mathrm{L}})\right]\right] = 0$$

Since the variance for a number is zero, the value of flux converges to the expected value,

$$\lim_{V\to\infty}\frac{1}{V}\left[([(G^k)_{i-1/2}]_{\mathrm{G}}) - ([(G^k)_{i-1/2}]_{\mathrm{L}})\right] = F_{i-1/2}^k,$$
$$\lim_{V\to\infty}\frac{1}{V}\left[([(G^k)_{i+1/2}]_{\mathrm{L}}) - ([(G^k)_{i+1/2}]_{\mathrm{G}})\right] = F_{i+1/2}^k. \tag{2.30}$$

Given, V being a positive non-zero number, multiply finite volume equation for particle number by $1/V$.

$$\begin{aligned}
{Q_{\mathrm{part}_i}}^{k+1} &= {Q_{\mathrm{part}_i}}^k - \frac{1}{V}\left([(G^k)_{i+1/2}]_{\mathrm{L}} + [(G^k)_{i-1/2}]_{\mathrm{L}}\right)\\
&\quad + \left([(G^k)_{i-1/2}]_{\mathrm{G}} + [(G^k)_{i+1/2}]_{\mathrm{G}}\right),\\
\lim_{V\to\infty}{Q_{\mathrm{part}_i}}^{k+1} &= Q_i^k - \lim_{V\to\infty}\frac{1}{V}\left[\left([(G^k)_{i+1/2}]_{\mathrm{L}} + [(G^k)_{i-1/2}]_{\mathrm{L}}\right)\right]\\
&\quad + \lim_{V\to\infty}\frac{1}{V}\left[\left([(G^k)_{i-1/2}]_{\mathrm{G}} + [(G^k)_{i+1/2}]_{\mathrm{G}}\right)\right].
\end{aligned}$$

Rearranging and then using equation (2.30),

$$\begin{aligned}
\lim_{\mathrm{V}\to\infty}{Q_{\mathrm{part}_i}}^{k+1} &= Q_i^k - \left(F_{i+1/2}^k - F_{i-1/2}^k\right)\\
\lim_{\mathrm{V}\to\infty}{Q_{\mathrm{part}_i}}^{k+1} &= Q_i^{k+1}.
\end{aligned}$$

From the principle of mathematical induction, since

$$\lim_{V\to\infty}{Q_{\mathrm{part}_i}}^{k+1} = Q_i^{k+1},$$

then the statement is true for all values of k (all time steps). This proves that the stochastic solution theoretically converges to the finite volume solution when $V\to\infty$ i.e. number of particles goes to infinity. □

This verifies that the stochastic formulation (FBPT) when applied to

a large number of particles converges to the finite-volume scalar solution (PST).

In this chapter, the general formulation for transport was discussed, and the link between PST and FBPT was established and theoretically verified. The FBPT method is executed for a finite number of time-steps, and Algorithm 1 is followed for updating the number of particles at the end of each time-step. Algorithm 2 is followed for the multinomial sampling of particles to calculate particle-flux values. In the following Chapter 3, explicit schemes for advection and diffusion are described and their numerical results will discussed in Chapter 5.

Algorithm 1 1D Particle Transport

1: Input : N^k,V {Particle Distribution in axial direction for timestep k and Sample volume}
2: Output : N^{k+1},Q^{k+1}_{part} {Particle Distribution and Particle concentration/density distribution in axial direction for timestep $k+1$ }
3: Define C_{adv} for selected explicit advection scheme (Chapter 3)
4: Define $C_{\text{diff}+}, C_{\text{diff}-}$ for selected explicit diffusion scheme (Chapter 3)
5: **for** Cell Number i = 1 to n_{x} **do**
6: calculate $[P^k_i]_{+x}$ and $[P^k_i]_{-x}$ from equation (2.20,2.21).
7: $P_{\text{R}} = [P^k_i]_{+x}$ and $P_{\text{L}} = [P^k_i]_{-x}$
8: $\{(G_{i+1/2})_{\text{S}}, (G_{i-1/2})_{\text{S}}\} \leftarrow \{P_{\text{R}}, P_{\text{L}}\}$ sampled using Algorithm 2.
9: **end for**{End of Iteration on all cells from 1 to n_{x}}
10: **for** Cell Number i = 1 to n_{x} **do**
11: $N^{k+1}_i = N^k_i - (G_{i+1/2})_{\text{S}} + (G_{i-1/2})_{\text{S}}$ {Calculating particle distribution for next time step}
12: **end for**{End of iteration for Updating new particle distribution}
13: $Q^{k+1}_{\text{part}} \leftarrow \frac{N^{k+1}}{V}$ {Particle concentration calculated from particle distribution}

Algorithm 2 Sampling of particles for 1D simulation

1: Input : N_i^k, $\{P_{\mathrm{R}}, P_{\mathrm{L}}\}$ {Particle Distribution in axial direction for timestep k, Probablities to move right or left}
2: Output : $(G_{i+1/2})_{\mathrm{S}}$ and $(G_{i-1/2})_{\mathrm{S}}$ {Particle flux in from both faces of cell i}
3: **for** All N_i^k, number of particles in cell i **do**
4: $r \leftarrow$ random number generator
5: **if** $r \leq P_{\mathrm{R}}$ **then**
6: $(G_{i+1/2})_{\mathrm{S}} = (G_{i+1/2})_{\mathrm{S}} + 1$ {Increments the flux for transferring that particle to its right cell}
7: **else** $\{P_{\mathrm{R}} < r \leq P_{\mathrm{R}} + P_{\mathrm{L}}\}$
8: $(G_{i-1/2})_{\mathrm{S}} = (G_{i-1/2})_{\mathrm{S}} - 1$ {Increments the flux for transferring that particle to its left cell}
9: **end if**
10: **end for**{End of iteration on set of particles in ith cell}

CHAPTER 3

EXPLICIT METHODS FOR STOCHASTIC PARTICLE-RESOLVED TRANSPORT

In the last chapter, a general formulation for the flux-based particle transport, FBPT, was discussed with its consistency as compared with finite-volume passive scalar transport, FV-PST. This chapter will begin with the basic constraints of explicit numerical methods. Next, this chapter will revisit some of the higher order advection and diffusion methods of FV-PST that can be implemented in FBPT method. Finally, a possible extension of the FBPT method for a two dimensional Cartesian grid will be proposed at the end of this chapter.

3.1 Constraints of explicit numerical methods

Numerical methods, which are explicit in time, do not have unbounded stability regions. The numerical explicit methods for advection are bound by local courant number (C_{u})[Moin, 2001]. Courant number for advection is defined as,

$$C_{\mathrm{u}} = u\frac{\triangle t}{\triangle x}.$$

$C_{\mathrm{u}} \leq 1$ states that a scalar quantity or a particle in a grid-cell i does not move more than a grid-cell in one time step. Hence, for keeping a valid probability model ($P \leq 1$), the time-step and the grid-spacing values are taken so that $C_{\mathrm{u}} \leq 1$. The Courant number defines the bounds on time-step for a given grid-spacing.

Similarly, for diffusion, the time-step bound varies as, $\triangle t \propto (\triangle x)^2$ and the proportionality constant is the diffusion coefficient in the medium. The stability here is defined by local diffusion number (C_{d}) [Moin, 2001] which is

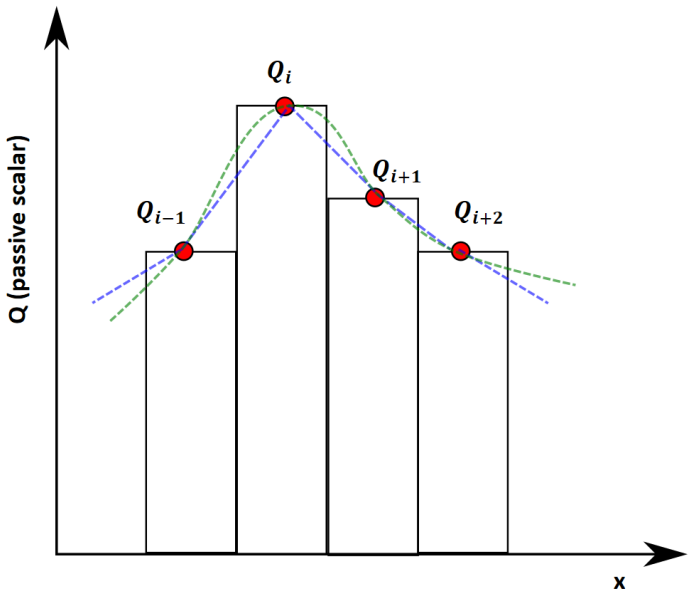

Figure 3.1: Schematic of a finite volume system. The dashed lines are the parametrization of the cell averaged data (in red). The default black line (piecewise constant) is used for a first order Upwind scheme. The blue line is used for a second order Piecewise linear scheme. The green line is a higher-order spline reconstruction.

given by,

$$C_{\mathrm{d}} = D_0 \frac{\triangle t}{\triangle x^2}.$$

For a valid probability model for our method, we need to ensure that the particles do not skip any grid-cell in a single time-step i.e. $(C_{\mathrm{u}} + C_{\mathrm{d}}) \leq 1$.

For transport in a finite-volume grid, the only data available is the cell average values of each grid cell. Different schemes use this data in different ways [Durran, 2013, Shu, 1998] as shown in Figure 3.1. For example, the Upwind advection scheme uses the piecewise-constant reconstruction which only require a one point stencil, while the piecewise linear schemes uses a linear reconstruction which requires a two point stencil. Some of these schemes for advection and diffusion will be discussed in the following sections.

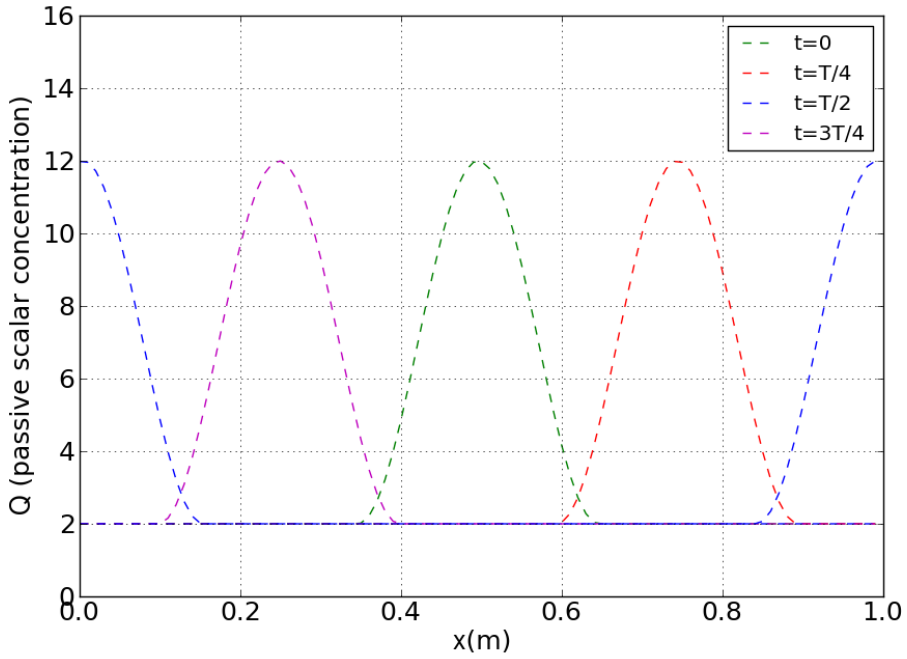

Figure 3.2: Analytical solution for advection equation (3.1) with periodic boundary, at $t = 0$, $t = T/4$, $t = T/2$ and $t = 3T/4$. Here T is one time period of the distribution. The distribution moves undistorted in x-direction.

3.2 Advection

Chapter 2 discussed the formulation of finite-volume methods for stochastic particle transport. The transport phenomena was classified into advection and diffusion processes. One dimensional advection equation for a scalar q is defined as equation (3.1),

$$\frac{\partial q}{\partial t} = -u\frac{\partial q}{\partial x}. \tag{3.1}$$

The analytical solution for the equation (3.1) is that the scalar q retains its shape while moving with a constant velocity. For example, if we consider a particle concentration distribution in one dimension as shown in Figure 3.2, the distribution moves undistorted in the x-direction in the presence of a finite velocity in x-direction provided the diffusion is absent. The scalar FV-PST method defines the advection flux as,

Table 3.1: Advection schemes with their order of accuracy(OA) for a constant Courant number

Flux Scheme	**OA**
Upwind Scheme	1
Piecewise Lin adv	2
Runge-Kutta 3	3

$$\mathbf{F}^k_{\text{adv}} = C_{\text{adv}}\mathbf{Q}^k. \tag{3.2}$$

The advection coefficient matrix C_{adv} defines the order of accuracy of the numerical method. Different schemes for solving the advection equation have been discussed extensively in previous literatures, e.g. Durran [2013]. Some of the schemes such as the Upwind scheme and the Piecewise-linear scheme have a fixed stencil for data reconstruction, whereas other schemes such as ENO and WENO [Shu, 1998], have a variable stencil to inhibit the oscillations caused in the numerical solution of the equation (3.1). In this thesis, we only consider the methods with fixed stencils as shown in Table 3.1.

One of the lower order popular finite volume schemes used for advection is the Upwind scheme. This scheme is first order accurate in both space and time, and follows a piecewise constant reconstruction of the cell average data. Although the scheme is consistent, it requires a very small time step and grid spacing to give an accurate solution.

The advection flux vector for the Upwind scheme on a staggered finite volume grid is given by,

$$(F^k_{\text{adv}})_{i+1/2} = \begin{cases} Q^n_i u^k_{i+1/2}\frac{\triangle t}{\triangle x} & u_{i+1/2} \geq 0 \\ Q^n_{i+1} u^k_{i+1/2}\frac{\triangle t}{\triangle x} & u_{i+1/2} < 0. \end{cases} \tag{3.3}$$

Corresponding probabilities, absent diffusion, for Upwind scheme as defined in equation (2.12) and (2.13) are given by,

$$[(P^k_{\text{adv}})_i]_{+\text{x}} = \begin{cases} u^k_{i+1/2}\frac{\triangle t}{\triangle x} & u_{i+1/2} \geq 0 \\ 0 & u_{i+1/2} < 0, \end{cases} \tag{3.4}$$

$$[(P^k_{\text{adv}})_i]_{-\text{x}} = \begin{cases} 0 & u_{i-1/2} \geq 0 \\ \left| u^k_{i-1/2} \frac{\triangle t}{\triangle x} \right| & u_{i-1/2} < 0. \end{cases} \tag{3.5}$$

Another scheme is the non-monotonic Piecewise linear scheme. This scheme is second order accurate in a uniform FV grid space, for pure advection with a constant courant number, and it uses piecewise-linear reconstruction of cell average data. The flux values for the Piecewise linear scheme are given by,

$$(F^k_{\text{adv}})_{i+1/2} = \begin{cases} r_{i-1/2} \left[Q^k_{i-1} + \frac{(1-r_{i-1/2})}{4} (Q^k_i - Q^k_{i-2}) \right] & u_{i+1/2} < 0 \\ r_{i+1/2} \left[Q^k_i + \frac{(1-r_{i+1/2})}{4} (Q^k_{i+1} - Q^k_{i-1}) \right] & u_{i+1/2} \geq 0, \end{cases} \tag{3.6}$$

$$r_{i-1/2} = u_{i-1/2} \frac{\triangle t}{\triangle x}.$$

The corresponding advection probability vector for piecewise-linear scheme is given by equation,

$$[(P^k_{\text{adv}})_i]_{+\text{x}} = \begin{cases} \frac{r_{i-1/2}}{N^k_i} \left[N^k_{i-1} + \frac{(1-r_{i-1/2})}{4} (N^k_i - N^k_{i-2}) \right] & u_{i+1/2} \geq 0 \\ 0 & u_{i+1/2} < 0, \end{cases} \tag{3.7}$$

$$[(P^k_{\text{adv}})_{i+1}]_{-\text{x}} = \begin{cases} 0 & u_{i+1/2} \geq 0 \\ \left| \frac{r_{i+1/2}}{N^k_{i+1}} \left[N^k_i + \frac{(1-r_{i+1/2})}{4} (N^k_{i+1} - N^k_{i-1}) \right] \right| & u_{i+1/2} < 0. \end{cases} \tag{3.8}$$

The higher-order advection methods in time can use multi-step time schemes or time-split methods. In Wicker and Skamarock [2002], a third order Runge-Kutta (RK3) scheme was implemented. This scheme is particularly relevant for this thesis because it has been implemented in WRF

transport model. For scalar advection, RK3 works in three steps as following:

$$\begin{aligned} Q_i^* &= Q_i^k - \frac{\triangle t}{3\triangle x}\left(F_{i+1/2}^k - F_{i-1/2}^k\right), \\ Q_i^{**} &= Q_i^k - \frac{\triangle t}{2\triangle x}\left({F_{i+1/2}^*}^k - {F_{i-1/2}^*}^k\right), \\ Q_i^{k+1} &= Q_i^k - \frac{\triangle t}{\triangle x}\left({F_{i+1/2}^{**}}^k - {F_{i-1/2}^{**}}^k\right). \end{aligned} \tag{3.9}$$

The expression of flux, F was defined for different spatial orders of discretization. For our analysis, we are using a fourth-order expression for flux in space,

$$\begin{aligned} F_{i-1/2} &= \frac{u_{i-1/2}}{12}[7(Q_i + Q_{i-1}) - (Q_{i+1} + Q_{i-2})], \text{or}, \\ \mathbf{F}^k &= C_{\text{adv}}\mathbf{Q}^k, \\ \mathbf{F}^{*k} &= C_{\text{adv}}\mathbf{Q}^{*k}, \\ \mathbf{F}^{**k} &= C_{\text{adv}}\mathbf{Q}^{**k}. \end{aligned} \tag{3.10}$$

The terms ${F_{i+1/2}^*}^k$, ${F_{i-1/2}^*}^k$, ${F_{i+1/2}^{**}}^k$ and ${F_{i-1/2}^{**}}^k$ are the components of the flux vectors $\mathbf{F}^{*k}$ and $\mathbf{F}^{**k}$ respectively. This method is third order accurate in time. RK3 scheme for particle transport can be defined as,

$$\begin{aligned} N_i^* &= N_i^k - \frac{\triangle t}{3\triangle x}\left(G_{i+1/2}^k - G_{i-1/2}^k\right), \\ N_i^{**} &= N_i^k - \frac{\triangle t}{2\triangle x}\left({G_{i+1/2}^*}^k - {G_{i-1/2}^*}^k\right), \\ N_i^{k+1} &= N_i^k - \frac{\triangle t}{\triangle x}\left({G_{i+1/2}^{**}}^k - {G_{i-1/2}^{**}}^k\right). \end{aligned} \tag{3.11}$$

This method is a three time-step method. The value $\mathbf{G}^{*k}$ is calculated analogous to $\mathbf{F}^{*k}$. Instead of sampling particles three times, the final step flux, $\mathbf{G}^{**k}$, is used for defining probabilities based on equation (2.12) and (2.13). Advection probabilities for RK-3 are given by,

$$[(P_{\text{adv}}^k)_i]_{+\text{x}} = \begin{cases} \left[\left(\frac{1}{N^{**k}_i}\right)\right]\{C_{\text{adv}}\mathbf{N}^{**k}\}_i & u_{i+1/2} \geq 0 \\ 0 & u_{i+1/2} < 0. \end{cases} \tag{3.12}$$

$$[(P^k_{\text{adv}})_i]_{-\text{x}} = \begin{cases} 0 & u_{i-1/2} \geq 0 \\ \left| \left[\left(\frac{1}{N^{**k}_i} \right) \right] \{C_{\text{adv}} \mathbf{N}^{**k}\}_{i-1} \right| & u_{i-1/2} < 0. \end{cases} \tag{3.13}$$

The particle flux is sampled according to the equation (2.14). For a finite velocity in x-direction (West to East), $G^k_{i+1/2} > 0$ and $G^k_{i-1/2} > 0$. All the simulations were performed for advection on the particle concentration distribution defined in Wicker and Skamarock [2002] with periodic boundary conditions. Numerical results for the test case 1D advection using all three schemes, with periodic boundary conditions, will be discussed in Chapter 5.

3.3 Diffusion

Diffusion is a random movement of particles with a time scale defined by diffusion coefficient in a medium. In absence of advection, pure diffusion equation for a passive scalar is given by,

$$\frac{\partial q}{\partial t} = \nabla \cdot (D_0 \nabla q) \tag{3.14}$$

The coefficient D_0 defines the time-scale associated with that of the process. For simplicity, we consider the diffusion coefficient, D_0, to be a constant. In one dimension,

$$\frac{\partial q}{\partial t} = D_0 \frac{\partial^2 q}{\partial x^2} \tag{3.15}$$

represents a parabolic diffusion equation. A schematic for diffusion process is described in Figure 3.3 where the distribution spreads out, due the process of diffusion, with time. Although some of the implicit schemes have been found to be unconditionally stable for diffusion problems, we are only going to consider explicit schemes because implicit implementation can be difficult for the formulation discussed in this work. When written in the same explicit flux based form as equation (2.5), the flux for scalar diffusion can be written as,

$$\mathbf{F}^k_{\text{diff}} = C_{\text{diff}} \mathbf{Q}^k, \tag{3.16}$$

Table 3.2: Diffusion schemes with their order of accuracy(OA) for a constant time-step($\triangle t$)

Flux Scheme	**Spatial OA**
2nd Order diffusion	2
4th Order diffusion	4

where C_{diff} depends on the spatial discretization used for the diffusion equation.

Second and fourth order diffusion were considered in this work for the demonstration of FBPT diffusion as shown in Table 3.2.

A second-order discretization of flux term is given by,

$$(F^k_{\text{diff}})_{i+1/2} = -D_0 \triangle t \frac{Q^k_i - Q^k_{i+1}}{\triangle x}. \tag{3.17}$$

As discussed in Chapter 2, for modeling the diffusion process of particles, the coefficient matrix C_{diff} is split into two parts. Hence, the probability for particle diffusion corresponding to the second order discretization is defined as,

$$[(P_{\text{diff}})^k_i]_{+\text{x}} = \left| \left[\left(\frac{1}{N^k_i} \right) \right] D_0 \triangle t \frac{N^k_i}{\triangle x} \right|, \tag{3.18}$$

$$[(P_{\text{diff}})^k_{i+1}]_{-\text{x}} = \left| \left[\left(\frac{1}{N^k_{i+1}} \right) \right] D_0 \triangle t \frac{N^k_{i+1}}{\triangle x} \right|. \tag{3.19}$$

The results for this will be discussed in Section 5.2.

Another scheme that can be used for diffusion is a fourth order scheme [Castillo et al., 2001] with the flux term given by ,

$$(F^k_{\text{diff}})_{i+1/2} = -D_0 \frac{1.125Q^k_i - 1.125Q^k_{i+1} + 0.041666Q^k_{i-1} - 0.041666Q^k_{i+2}}{\triangle x}. \tag{3.20}$$

Probability values were found in the same way as in equation (2.17),

$$[(P_{\text{diff}})^k_i]_{+\text{x}} = \left[\left(\frac{1}{N^k_i} \right) \right] \left| D_0 \frac{1.125N^k_i + 0.041666N^k_{i-1}}{\triangle x} \right|, \tag{3.21}$$

$$[(P_{\text{diff}})^k_{i+1}]_{-\text{x}} = \left[\left(\frac{1}{N^k_{i+1}} \right) \right] \left| D_0 \frac{1.125N^k_{i+1} + 0.041666N^k_{i+2}}{\triangle x} \right|. \tag{3.22}$$

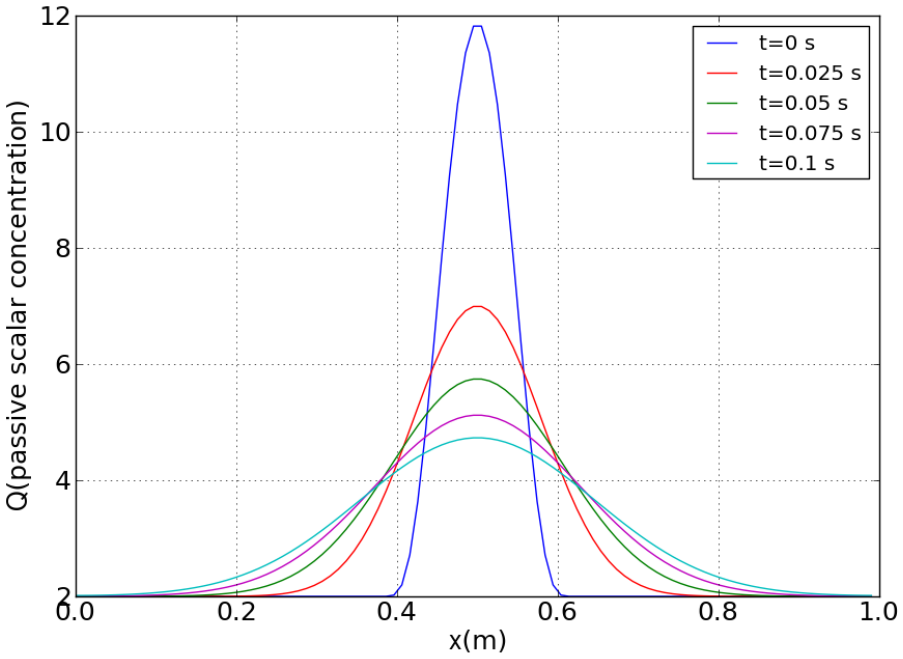

Figure 3.3: Diffusion with second order diffusion scheme at $t = 0$, $t = 0.025\ s$, $t = 0.05\ s$, $t = 0.075\ s$ and $t = 0.1\ s$. This result is for $D_0 = 0.01\ \mathrm{m}^2/\mathrm{s}$ and $n_\mathrm{x} = 101$.

As the diffusion process proceeds in time, the distribution 'evens out' as shown in Figure 3.3.

For analysis purposes, a test case of particle distribution in the shape of a piecewise-constant wave was simulated with a constant diffusion coefficient. The analytical solution for a constant diffusion-coefficient piecewise-constant-wave problem is known and was compared with the stochastic method (FBPT) solution. The results for the test case will be discussed in Section 5.2.

3.4 Extension of stochastic transport for a two-dimensional grid

Scalar transport for a 2D structured grid in finite volume was discussed in Chapter 2. There are a number of ways to perform the task, among which operator splitting method and direct flux methods are most popular [Takacs, 1985]. We are not going to present a full analysis of a 2D problem in this work

but an extension is straightforward and can be applied using the formulation for a 1D grid.

The passive scalar transport equation for a 2D grid of X-Y Cartesian coordinate system is given by equation (2.4),

$$\begin{aligned}\frac{\partial q}{\partial t} &= -\nabla \cdot (uq) + (\nabla \cdot D_0(\nabla q)).\\ \frac{\partial q}{\partial t} &= -\frac{\partial (u_{\mathrm{x}} q)}{\partial x} - \frac{\partial (u_{\mathrm{y}} q)}{\partial y} + \frac{\partial}{\partial x}\left[D_0 \frac{\partial q}{\partial x}\right] + \frac{\partial}{\partial y}\left[D_0 \frac{\partial q}{\partial y}\right], \end{aligned} \tag{3.23}$$

and the finite volume form of the passive scalar transport equation is given by equation (2.5). The stochastic particle transport formulation in a 2D grid will have four independent events for a particle in a grid cell. Each event corresponds to the particle going through one of the four faces as shown in Figure 2.2. The 1D formulation discussed in Chapter 2 can be extended to apply it for a 2D grid. Assuming the X and Y direction transport are independent, probabilities $[P^k_{i,j}]_{+\mathrm{x}}$,$[P^k_{i,j}]_{-\mathrm{x}}$,$[P^k_{i,j}]_{+\mathrm{y}}$ and $[P^k_{i,j}]_{-\mathrm{y}}$ can be calculated by defining an algorithm to consider one-slab at a time as shown in Figure 3.4. Indices (i, j) represent the grid-cell on the 2D grid.

The particle population at the next time step is defined as,

$$N^{k+1}_{i,j} = N^k_{i,j} + \left(\sum_{s=1}^{k} (G^k_s)\right), \tag{3.24}$$

where k represents the total number of faces a particle from a grid-cell can be transported. Similar to the previous hypothesis regarding sampling of particles to calculate fluxes, 2D fluxes can be calculated as,

$$\{G^k_{\mathrm{s}}\}_{i,j} = \mathrm{multinomial}(N^k_{i,j}, \{P^k_{\mathrm{s}}\}_{i,j}), \tag{3.25}$$

where $\{P^k_{\mathrm{s}}\}_{i,j}$ represents the set of probabilities of a particle in the direction of corresponding faces. For the case of a structured grid, $\{P^k_{\mathrm{s}}\}_{i,j}$ comprises $[P^k_{i,j}]_{+\mathrm{x}}$,$[P^k_{i,j}]_{-\mathrm{x}}$,$[P^k_{i,j}]_{+\mathrm{y}}$ and $[P^k_{i,j}]_{-\mathrm{y}}$.

There are other different ways to design an algorithm to calculate the set $\{P_{\mathrm{s}}\}_{i,j}$. Probabilities can also be calculated using operator splitting between x and y directions for transport and a qualitative result has been shown in Figure 6.1.

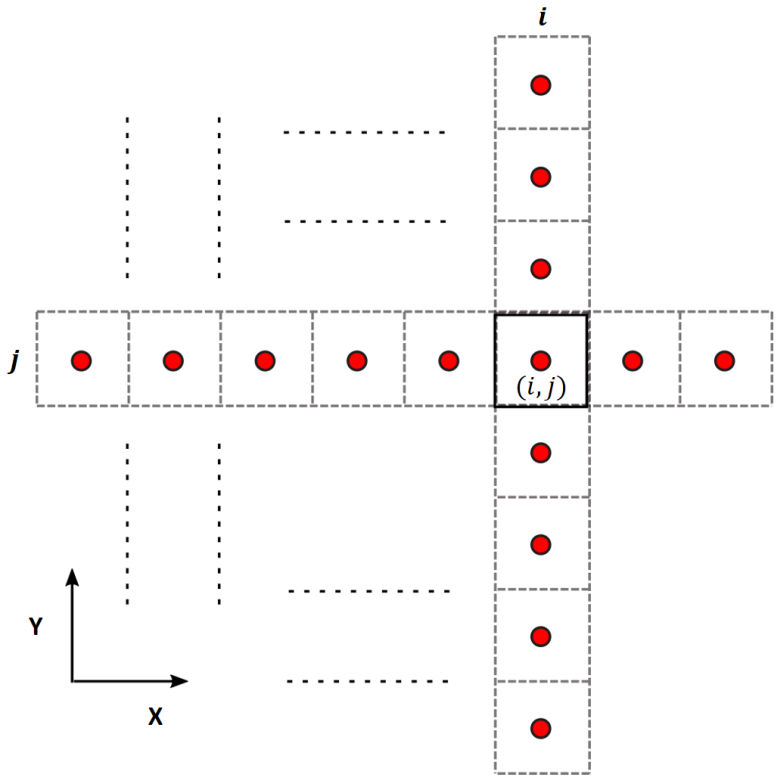

Figure 3.4: Stochastic Transport in a 2D structured grid. The indices i and j represent the vertical and horizontal slabs respectively.

CHAPTER 4

ERROR ANALYSIS

In this chapter, segregation and convergence of error for FBPT will be discussed. Since the coefficient matrix used to define probabilities is same as the finite-volume passive scalar transport (FV-PST) coefficient matrix, the stability conditions for stochastic methods are the same as for the corresponding FV scheme.

Errors in finite-volume advection are classified as (1) Dissipation error and (2) Dispersion error. The dissipation error occurs due to the leading truncation term in the Taylor series expansion of scheme is of even order. From Figure 4.1, the upwind scheme introduces a huge numerical diffusion error which acts to reduce the amplitude of the scalar distribution. The dispersion error occurs when leading truncation error term is of odd order. This causes a phase-lag in the scalar distribution as shown in Figure 4.2. The previous literatures on advection schemes [Crowley, 1968, Takacs, 1985] discuss the quantification of these errors, but these errors will not be discussed further in this work and will be labeled as finite-volume error e_{FV}.

4.1 Segregation of error

Errors were computed in comparison to the analytical solution for the advection equation. By defining the particle concentration, the total error in a grid-cell i at time-step k can be split into finite-volume error and stochastic

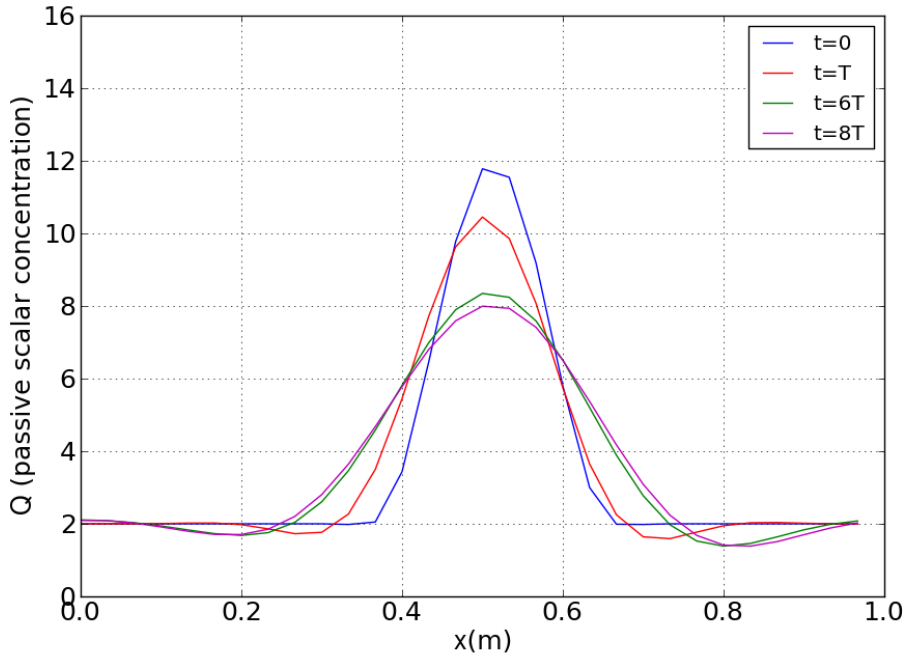

Figure 4.1: Advection with Piecewise linear scheme at $t = T$, $t = 6T$ and $t = 8T$ displaying dispersion error. This result is for $n_{\mathrm{x}} = 30$ and $t = T$ is the period of the distribution to move across the domain once.

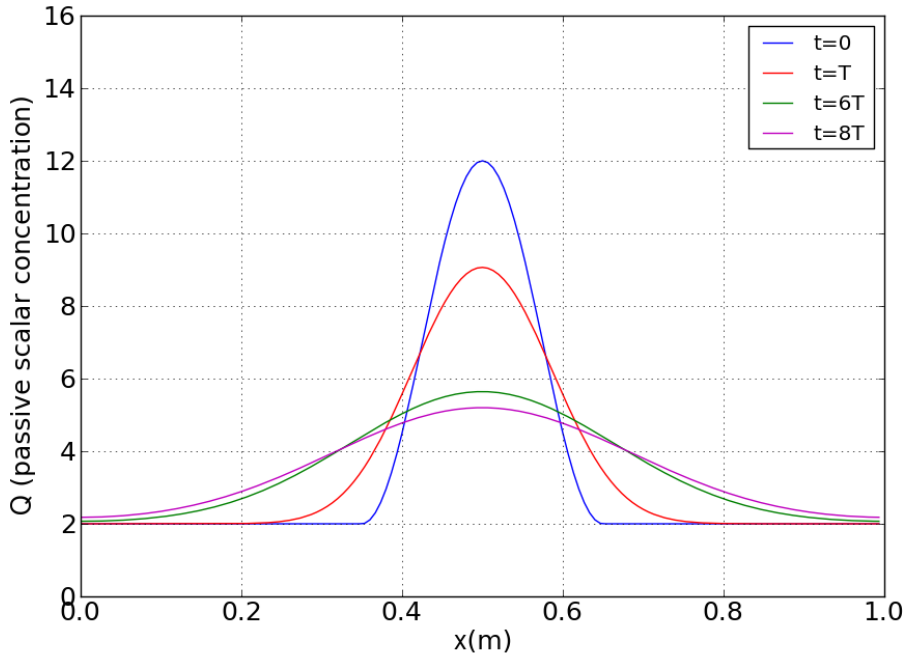

Figure 4.2: Advection with Upwind scheme at $t = 0$, $t = T$, $t = 6T$ and $t = 8T$ displaying dissipation error. This result is for $n_{\mathrm{x}} = 150$ and $t = T$ is the period of the distribution to move across the domain once.

error.

$$
\begin{aligned}
{Q_{\text{part}}}_i^k &= \frac{N_i^k}{\mathrm{V}}, \\
e_i^k &= {Q_{\text{part}}}_i^k - {Q_{\text{analytical}}}_i^k, \\
e_i^k &= \underbrace{{Q_{\text{part}}}_i^k - Q_i^k}_{{e_{\mathrm{S}}}_i^k} + \underbrace{Q_i^k - {Q_{\text{analytical}}}_i^k}_{{e_{\mathrm{FV}}}_i^k}, \\
e_i^k &= {e_{\mathrm{S}}}_i^k + {e_{\mathrm{FV}}}_i^k.
\end{aligned}
$$

Here, V is the sample volume (constant for a simulation). The variables, Q_{part} and $Q_{\text{analytical}}$, were compared for error estimation. Also, here ${e_{\mathrm{S}}}_i^k$ refers to the stochastic error and ${e_{\mathrm{FV}}}_i^k$ refers to the finite volume error for the method. From Theorem 1, we recall that

$$
\begin{aligned}
\mathrm{E}[e_i^k] &= \mathrm{E}({e_{\mathrm{S}}}_i^k) + \mathrm{E}({e_{\mathrm{FV}}}_i^k), \\
\mathrm{E}[e_i^k] &= {e_{\mathrm{FV}}}_i^k.
\end{aligned} \tag{4.1}
$$

However, to account for stochastic standard deviation along with finite volume error, root-mean-square (RMS) values of the total error for a time can be computed. The RMS value of the total error at a time step k is given by,

$$
\begin{aligned}
e_{\text{RMS}}^k &= \sqrt{\frac{\sum_{i=1}^{n_{\mathrm{x}}}[e_i^k]^2}{n_{\mathrm{x}}}}, \\
e_{\text{RMS}}^k &= \sqrt{\frac{\sum_{i=1}^{n_{\mathrm{x}}}[{e_{\mathrm{S}}}_i^k + {e_{\mathrm{FV}}}_i^k]^2}{n_{\mathrm{x}}}}, \\
[e_{\text{RMS}}^k]^2 &= \frac{\sum_{i=1}^{n_{\mathrm{x}}}[{e_{\mathrm{S}}}_i^k + {e_{\mathrm{FV}}}_i^k]^2}{n_{\mathrm{x}}}, \\
\mathrm{E}([e_{\text{RMS}}^k]^2) &= \frac{1}{n_{\mathrm{x}}}\sum_{i=1}^{n_{\mathrm{x}}}[\mathrm{E}([{e_{\mathrm{S}}}_i^k]^2) + \mathrm{E}([{e_{\mathrm{FV}}}_i^k]^2) + 2\mathrm{E}[({e_{\mathrm{S}}}_i^k)({e_{\mathrm{FV}}}_i^k)]], \\
\mathrm{E}([e_{\text{RMS}}^k]^2) &= \frac{1}{n_{\mathrm{x}}}\sum_{i=1}^{n_{\mathrm{x}}}\left[(\sigma({e_{\mathrm{S}}}_i^k))^2 + ({e_{\mathrm{FV}}}_i^k)^2 + 2({e_{\mathrm{FV}}}_i^k)\mathrm{E}[({e_{\mathrm{S}}}_i^k)]\right], \\
\mathrm{E}([e_{\text{RMS}}^k]^2) &= \frac{1}{n_{\mathrm{x}}}\sum_{i=1}^{n_{\mathrm{x}}}[({e_{\mathrm{FV}}}_i^k)^2 + (\sigma({e_{\mathrm{S}}}_i^k))^2].
\end{aligned} \tag{4.2}
$$

Since the RMS value of the total error gives the standard deviation term along with the finite-volume error, it was used for error analysis and convergence study.

4.2 Convergence of error

The convergence of total root-mean-square error depends on the number of particles in the domain which depends on the parameter V, the sample volume. The only stochastic element in equation (4.2) is the last term. Since the probabilities in the equations for the fluxes depend on the number of particles to be sampled, calculating the exact standard deviation expression can be mathematically difficult. However, it can be remarked that the root-mean-square error is proportional to $1/\sqrt{V}$.

Theorem 3. *If the initial particle population distribution is defined as,*

$$N_i^0 = VQ_i^0,$$
$$Q_{\text{part}}{}_i^k = \frac{N_i^k}{V},$$

and the flux through faces is defined as,

$$\{[(G^k)_{i-1/2}]_{\text{L}}, [(G^k)_{i+1/2}]_{\text{L}}\} \sim \text{multinomial}(N_i^k, [(P)_i^k]_{-\text{x}}, [(P)_i^k]_{+\text{x}}),$$

then the expected value of variance of stochastic error depends on V as,

$$\text{E}\left[\sigma^2[e_{\text{S}}{}_i^k]\right] \propto \frac{1}{V}. \tag{4.3}$$

Proof. The unknown term in equation (4.2) is the second term on the RHS. Since we are not looking for an exact expression of standard deviation, but only its dependence on V, the non-stochastic variables, Q_i^k, are eliminated since they do not contribute to the standard deviation dependence on V. Standard deviation for stochastic error, e_{S} is given by,

$$\sigma^2[e_{\text{S}}{}_i^k] = \sigma^2[Q_{\text{part}}{}_k^i - Q_k^i],$$
$$\sigma^2[e_{\text{S}}{}_i^k] \simeq \sigma^2[Q_{\text{part}}{}_i^k]. \tag{4.4}$$

Since the p.d.f. of flux G is given by multinomial sampling with given population distribution of previous time step N^k, the standard deviation for a flux is given by,

$$\sigma^2([(G^k)_{i-1/2}]_{\mathrm{L}}|\mathbf{N}^k) = N_i^k[(P)_i^k]_{-\mathrm{x}}(1 - [(P)_i^k]_{-\mathrm{x}}),$$

A similar expression can be written for all other three fluxes. As proved in Theorem 1, the expected value of particle population, $\mathrm{E}[N_i^k] \propto V$. Also, since expression of P has N_i^k in numerator and denominator, the probabilities have a neutral dependence on V.

$$\mathrm{E}\left[\sigma^2([(G^k)_{i-1/2}]_{\mathrm{L}}|\mathbf{N}^k)\right] = \mathrm{E}[N_i^k][(P)_i^k]_{-\mathrm{x}}(1 - [(P)_i^k]_{-\mathrm{x}}),$$

$$\mathrm{E}\left[\sigma^2[G^k|\mathbf{N}^k]\right] \propto V,$$

for a generic flux G. This states that for a given time-step particle population distribution $\mathbf{N}^k$ the mean value of $\sigma^2[G^k] \propto V$. Since the value of V is a constant through all time steps, we can conclude that,

$$\mathrm{E}\left[\sigma^2[G^k]\right] \propto V.$$

Also, $\sigma^2[{Q_{\mathrm{part}}}_i^k]$ depends on $\sigma^2[G^k]/V^2$ and hence,

$$\mathrm{E}\left[\sigma^2[e_{\mathrm{S}}{}_i^k]\right] \simeq \mathrm{E}\left[\sigma^2[{Q_{\mathrm{part}}}_i^k]\right] \propto \frac{1}{V}.$$

□

Remark. *From Theorem 3 and equation 4.2, we can say that for* $e_{\mathrm{FV}}^2 \ll \sigma^2[e_{\mathrm{S}}{}_i^k]$,

$$\mathrm{E}\left[(e_{\mathrm{RMS}}^k)^2\right] \propto \frac{1}{V}.$$

Hence the square of root-mean-square of total error is inversely proportional to the sample volume (V) i.e. total number of particles.

Hence it can be conjectured that on a logarithmic plot for e_{RMS} vs V, the linear region should have a slope of $(-1/2)$. This result is consistent with the Monte-Carlo methods which also have a convergence of $(-1/2)$ w.r.t. the

number of support points [Haghighat, 2014]. In the following chapter, the numerical results for explicit methods with their error convergence will be discussed.

CHAPTER 5

NUMERICAL RESULTS

In this chapter, the numerical results for flux-based particle transport, FBPT, and their comparison with finite-volume passive scalar transport, FV-PST, will be discussed. The results for one dimensional advection and diffusion will be shown for some test cases. The convergence analysis of these tests will be discussed at the end of this chapter.

5.1 1D advection tests

Particle stochastic transport simulations were performed with various initial conditions for particle concentration. The results presented in this section are for modified initial conditions from Wicker and Skamarock [2002],

$$Q_{\text{part}}(x,0) = \begin{cases} 2 + (1 + \exp[80(|x - 0.5| - 0.15)])^{-1} & x \in (0,1) \\ 2 & otherwise, \end{cases} \tag{5.1}$$

The initial conditions were modified by adding a constant value of 2 to keep FV-PST values positive.

For an aerosol transport simulation, all the particles are distinct from each other. Since the only aspect considered in our problem is the number concentration of particles, all particles were treated identical to each other for computing results and then the number concentration was compared with the analytical solution. The initial particle population distribution was given by,

$$N(x,0) = \begin{cases} 2V + V(1 + \exp[80(|x - 0.5| - 0.15)])^{-1} & x \in (0,1) \\ 2V & otherwise, \end{cases} \tag{5.2}$$

where V, sample volume, was defined in Section 2.4. The 1D advection prob-

lem was solved using a constant velocity $u = 1$ m/s with periodic boundary conditions on both boundaries. Courant number, $C_{\mathrm{u}} = 0.4$, was used for all the advection results shown in the section. The period of a distribution is defined as the time taken by a particle to return to its initial position when domain has periodic boundary conditions. The period of the particle distribution in this test case, $T = 1$ s. The Upwind, the Piecewise-Linear and the RK3 explicit schemes [Durran, 2013] were implemented with the appropriate coefficient matrix, C_{adv}, for the flux-based stochastic particle transport, FBPT. These results from FBPT will be compared with FV-PST results in the following sections.

Figure 5.1 shows FV-PST results for three advection schemes which we will use as a reference for comparison with FBPT results. Each scheme introduces a different type of error depending on which modes it suppresses and which modes can sustain or grow [Durran, 2013].

Figure 5.2 shows results for the particle concentration distribution at times $t = 0$, $t = T/2$, $t = 3T/4$ and $t = T$ on a grid with $n_{\mathrm{x}} = 100$ for different values of V when the Upwind scheme is used. These results represent the simulation run for one realization (i.e. it is not the average of multiple runs to collect statistical data). This figure demonstrates that the particle concentration (stochastic) converges towards scalar concentration (finite volume) as V increases. A similar trend is observed for the piecewise linear scheme, shown in Figure 5.3, and the RK-3 scheme, shown in Figure 5.4. These results are in agreement with Theorem 2.

For the error analysis of the test cases, one hundred realizations were performed to calculate the mean (expected) value of particle concentration and the corresponding standard deviation.

5.2 1D diffusion tests

To test our diffusion algorithm, we consider a population of particles in a 1D grid with wall (zero gradient) boundary conditions as shown in Figure 2.6. The diffusion process, when observed for a long time, leads the particle population to an equilibrium state when the variance in particle distribution reaches a constant value.

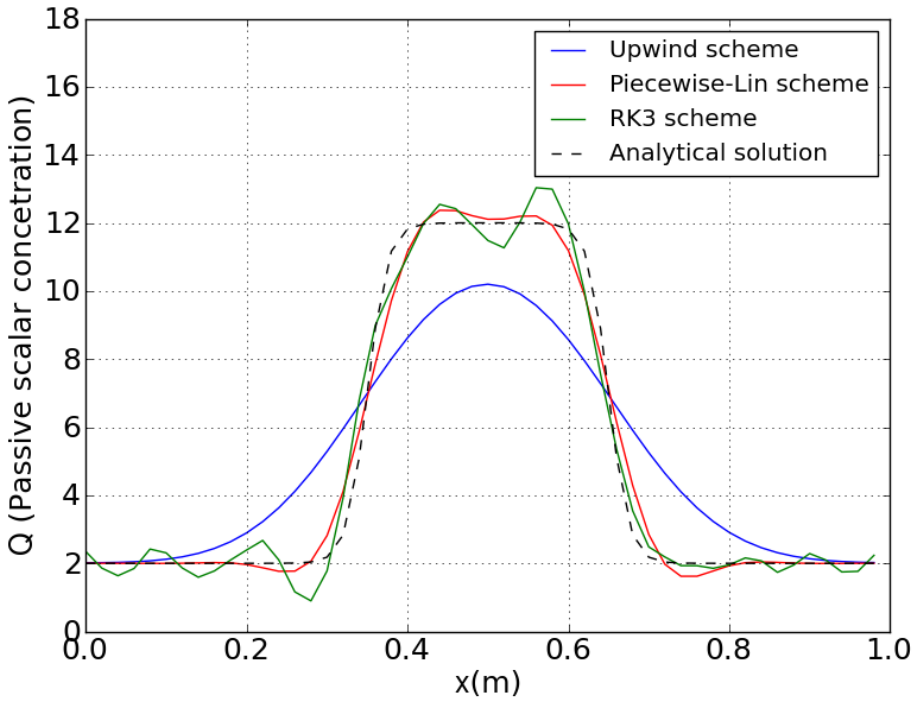

Figure 5.1: Numerical advection of a passive scalar (PST) for different schemes with analytical solution (dashed line) at $t = T$. Here $n_{\mathrm{x}} = 50$ and $C_{\mathrm{u}} = 0.4$.

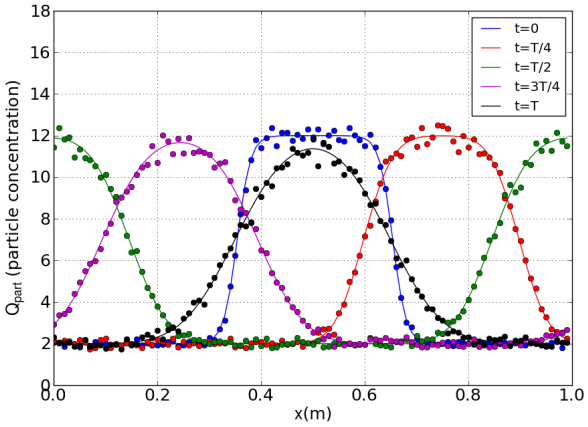

(a) $V = 100$

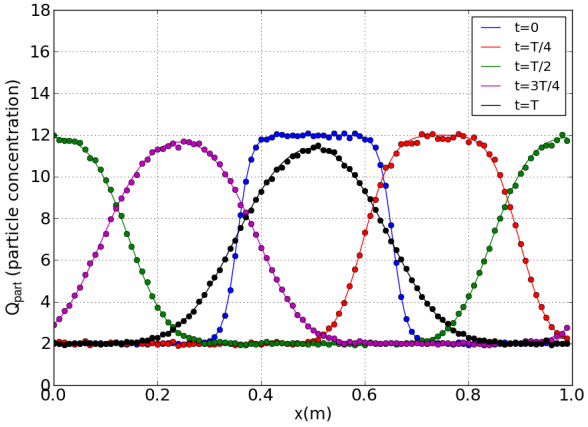

(b) $V = 1000$

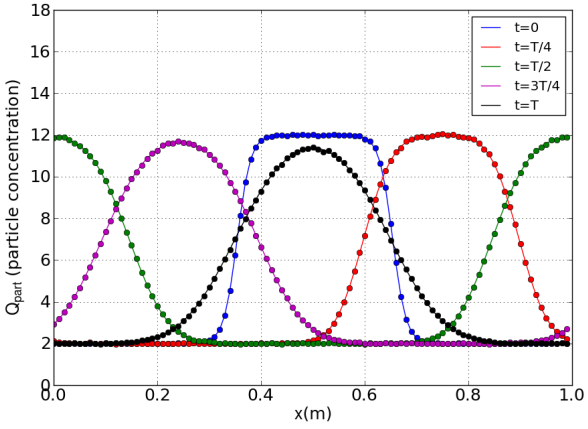

(c) $V = 10000$

Figure 5.2: Advection results for Upwind scheme. Solid line represents the PST results and bubbles represent the particle concentration (FBPT) stochastic simulation result. Here, $n_{\mathrm{x}} = 100$ and $C_{\mathrm{u}} = 0.4$.

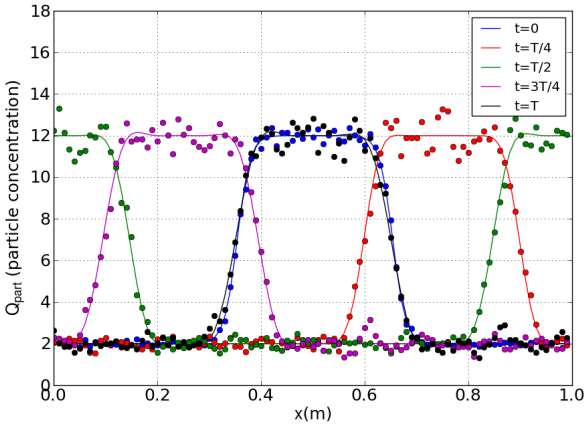

(a) $V = 100$

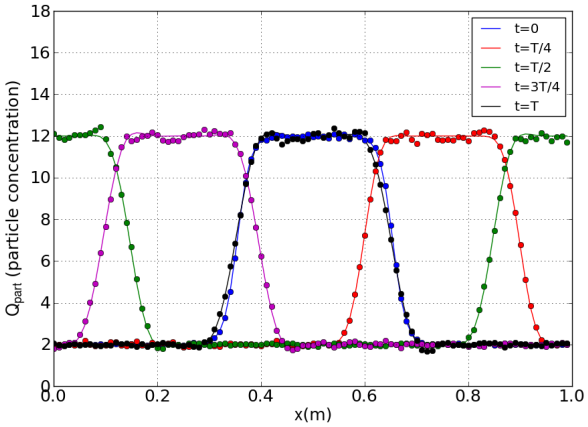

(b) $V = 1000$

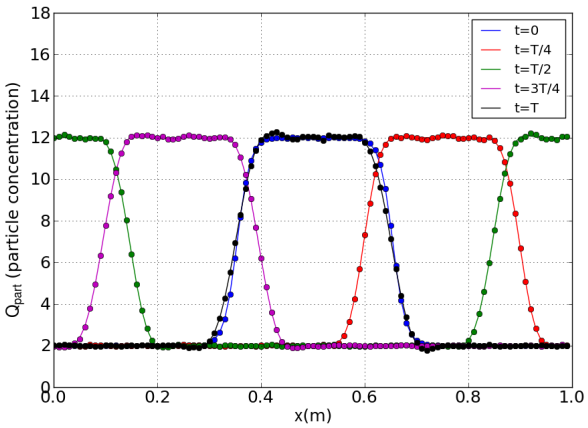

(c) $V = 10000$

Figure 5.3: Advection results for Piecewise-Linear scheme. Solid line represents the PST results and bubbles represent the particle concentration (FBPT) stochastic simulation result. Here, $n_{\mathrm{x}} = 100$ and $C_{\mathrm{u}} = 0.4$.

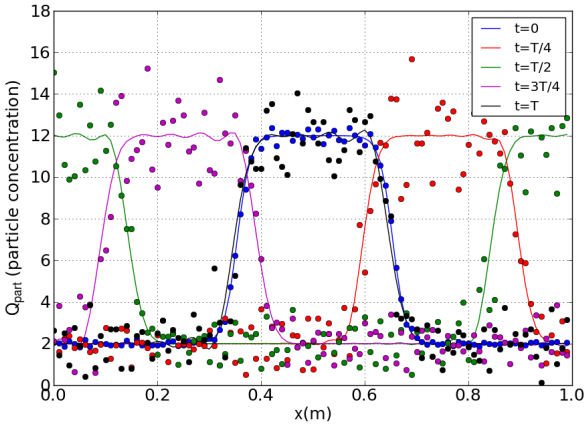

(a) $V = 100$

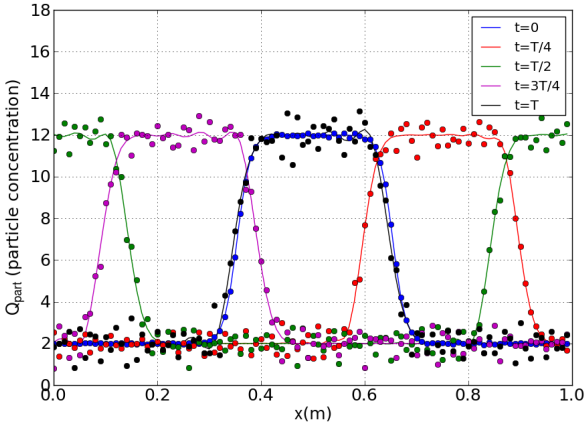

(b) $V = 1000$

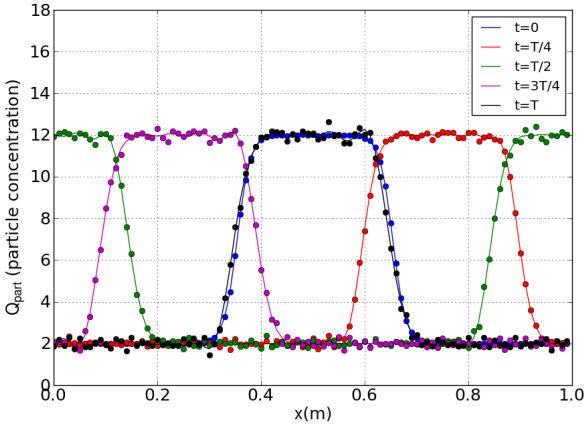

(c) $V = 10000$

Figure 5.4: Advection results for RK3 scheme. Solid line represents the PST results and bubbles represent the particle concentration (FBPT) stochastic simulation result. Here, $n_{\mathrm{x}} = 100$ and $C_{\mathrm{u}} = 0.4$.

Conjecture 1. *For $t \to \infty$, a particle is equally likely to be in any of the grid-cells. The particle population in a grid cell is given by,*

$$\lim_{t\to\infty} N_i^k \sim \text{binomial}\left(N_{\text{tot}}, \frac{1}{n_{\text{x}}}\right),$$
$$\lim_{t\to\infty} \sigma(N_i^k) = \sqrt{N_{\text{tot}} \frac{1}{n_{\text{x}}}\left(1 - \frac{1}{n_{\text{x}}}\right)}. \tag{5.3}$$

where, N_{tot} is the total number of particles in the domain.

This conjecture is supported by the numerical evidence shown in Figure 5.5, where the mean standard deviation (MSD) of a 1D grid converges towards the conjectured value of 3.704 calculated from equation (5.3). Wall boundary conditions were used for this test, and the particle population distribution for the case was mentioned in Figure 2.6. Since the error tolerance required for the standard deviation was low, 3000 realizations were run for this test.

We also investigated the transient behavior of particles due to diffusion. Stochastic method for diffusion, absent advection, was performed on a piecewise-constant wave function with wall boundary conditions and was compared with the analytical solution [Csanady, 2012],

$$N(x,t) = \frac{N_0}{2}\left[\text{erf}\left(\frac{r_0 + (x - 0.5)}{\sqrt{4D_0 t}}\right) + \text{erf}\left(\frac{r_0 - (x - 0.5)}{\sqrt{4D_0 t}}\right)\right] \tag{5.4}$$

where N_0 and r_0 represent the amplitude of the piecewise-constant wave and the half-width of the distribution respectively. The results for a second order diffusion with $N_0 = 14$ and $r_0 = 0.1$ are shown in Figure 5.6. The results for fourth order diffusion were very similar and almost indistinguishable to the second order results for the given test case.

5.3 Convergence analysis

As observed in Sections 5.1 and 5.2, the total error reduces with increasing number of particles per grid cell. The errors involved were quantified in Chapter 4.

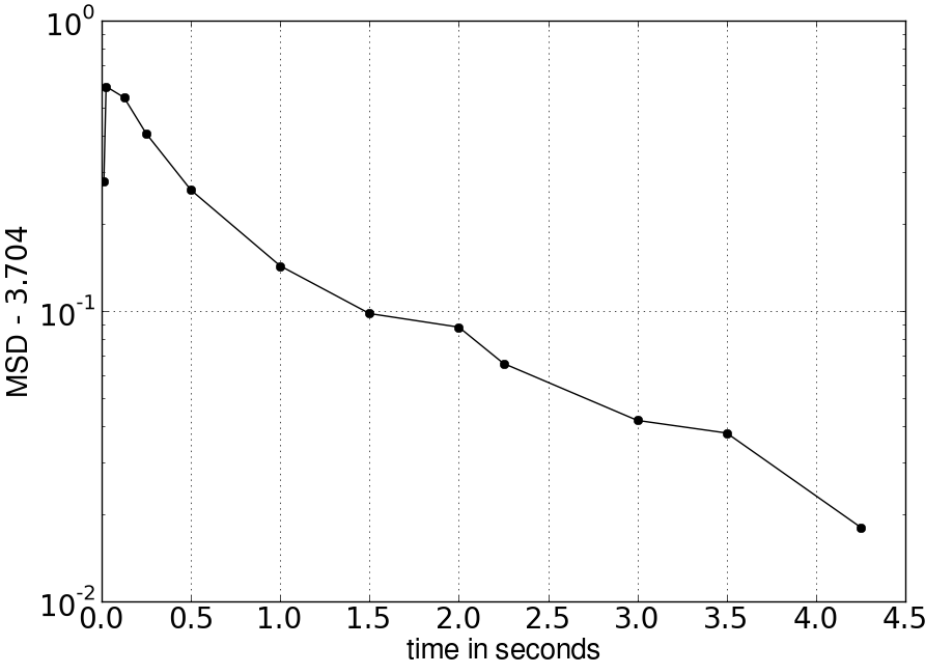

Figure 5.5: (Mean standard deviation(MSD) - $\sigma_{\text{Theoritical}}$) of particle population in a grid ($n_{\text{x}} = 50$) with time(sec). $D_0 = 0.08$ m^2/s was used for the case. The theoretical value of $\sigma_{\text{Theoritical}} = 3.704$ was calculated from equation (5.3).

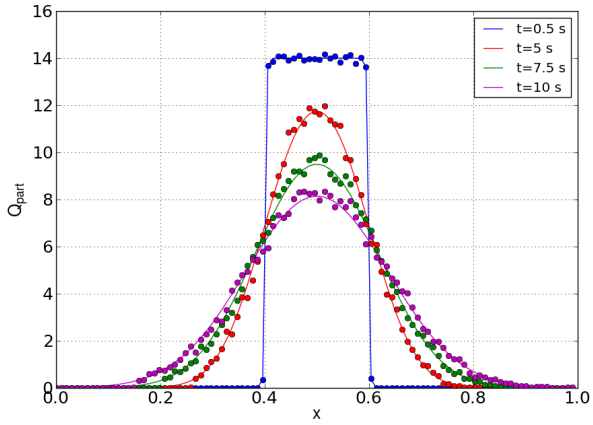

(a) $V = 100$

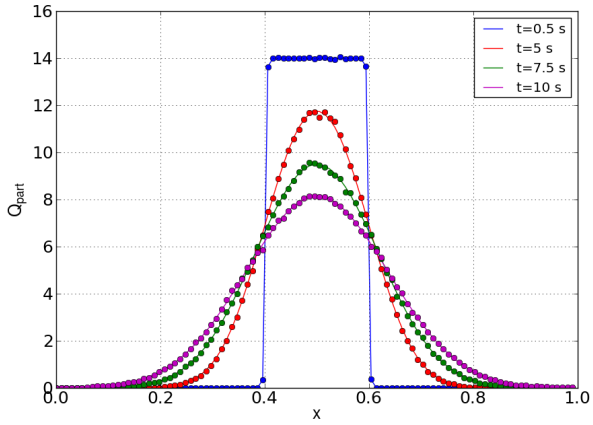

(b) $V = 1000$

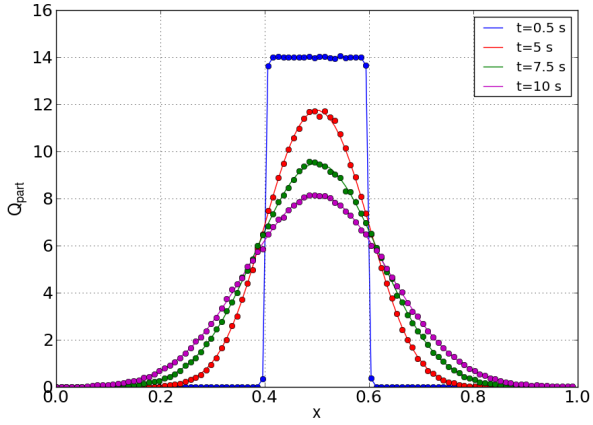

(c) $V = 10000$

Figure 5.6: Diffusion results for second order scheme. Solid line represents PST results and bubbles represent the particle concentration (FBPT) stochastic simulation result. Here, $n_{\mathrm{x}} = 101$, $\triangle t = 0.0025s$ and $D_0 = 0.001$ m^2/s.

The RMS values of total error (e_i^k) were calculated at $t = T$ (Time-period) for advection for the Upwind, the Piecewise Linear and the RK3, and then plotted against V in Figure 5.7, 5.8 and 5.9 respectively. Similarly, the RMS values of total error for diffusion were calculated for $t = 3$ sec with the same constants (N_0 and r_0) as mentioned above. Second-order and fourth-order diffusion RMS error is shown in Figure 5.10.

It is observed in all of the above mentioned figures that e_{RMS} is proportional to $1/\sqrt{V}$ for small values of V, which was remarked in Theorem 3 of Chapter 4. The convergence plot reaches a saturation (flat region) for large values of V because the second term (standard deviation) in equation (4.2) decreases with V and the RMS error, e_{RMS}, approaches a constant value of $(e_{\text{FV}})_{\text{RMS}}$ i.e. the flat region. This observation is found in both advection and diffusion results.

As described above, since the second term of equation (4.2) diminishes with large values of V, e_{RMS} values moves towards root-mean-square values of finite volume scalar transport, $(e_{\text{FV}})_{\text{RMS}}$. This is illustrated in Figure 5.11 where e_{RMS} values (in circles) are co-plotted with $(e_{\text{FV}})_{\text{RMS}}$ values (in solid) of various advection schemes for $V = 10^4$ or $V = 10^5$ (depending on when they approached saturation) and these values are close to their corresponding finite volume methods. It can also be observed that the values for high-resolution grid show some deviation from FV values. The deviation of the circles (FBPT) from the solid line (FV-PST) is because for the high grid resolution (high n_{x}), $(e_{\text{FV}})_{\text{RMS}}$ is lower and the plots shown in Figure 5.7, 5.8 and 5.9 have not reached a saturation for $V = 10^4, 10^5$. We can see from Figure 5.11 that the Upwind scheme RMS values reached saturation at $V = 10^4$ and coincides with FV-PST values, the Piecewise-linear scheme RMS values are very close to FV-PST at $V = 10^5$ and some RMS values of the RK-3 ($n_{\text{x}} = 100, 150, 250$) scheme did not reach a saturation/flat region at $V = 10^5$ and hence are away from the corresponding FV-PST values.

The grid-convergence plot shown in Figure 5.11 confirms that for advection process, the Upwind scheme, the the Piecewise-linear scheme and the Runge-Kutta 3 scheme have a grid convergence of the order one, two and three, respectively, for high grid-resolution.

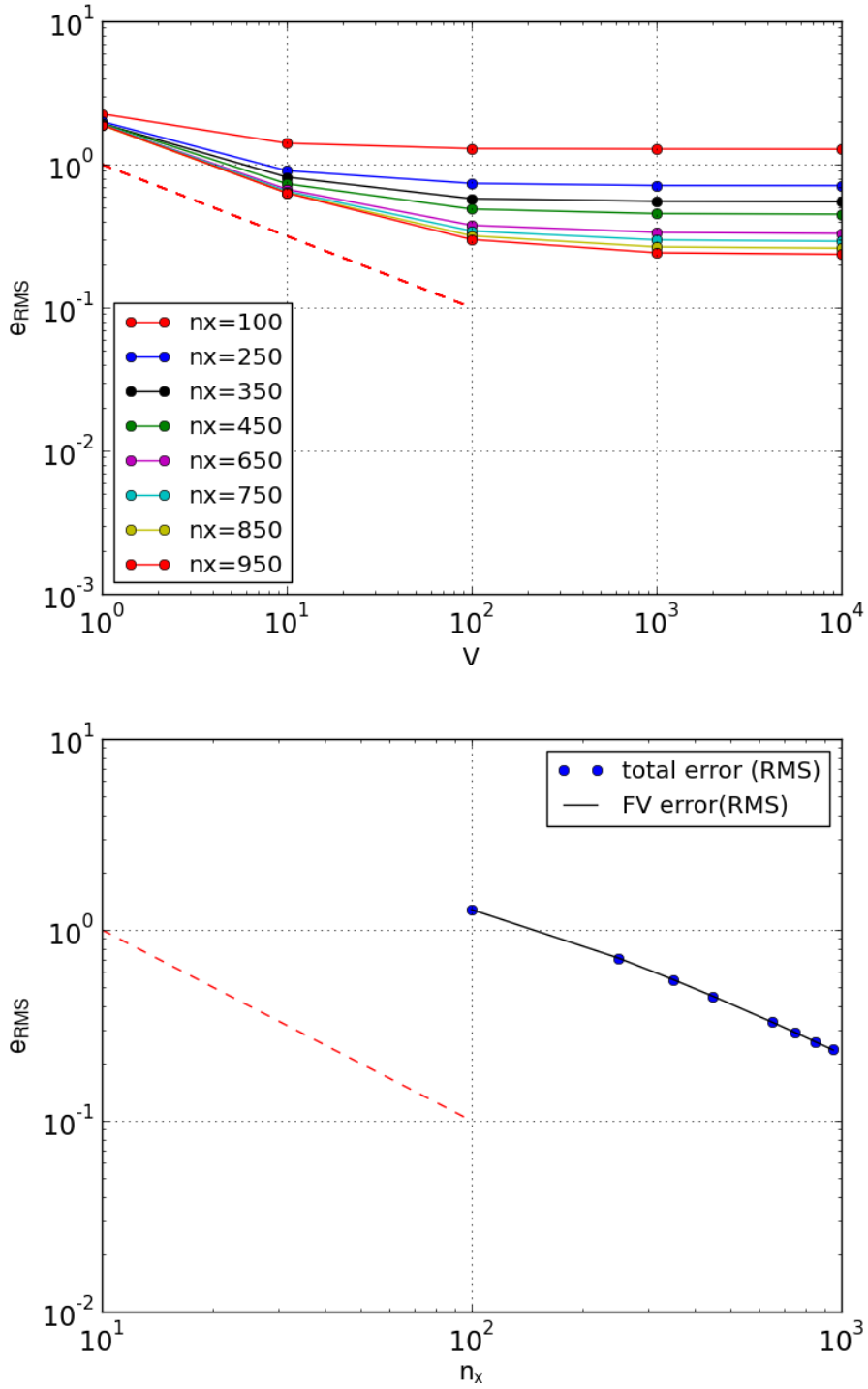

Figure 5.7: e_{RMS} variation with V and n_{x} for advection using Upwind scheme. Dashed line represents a line with slope of $(-1/2)$ in the figure on top and slope (-1) in figure in the bottom.

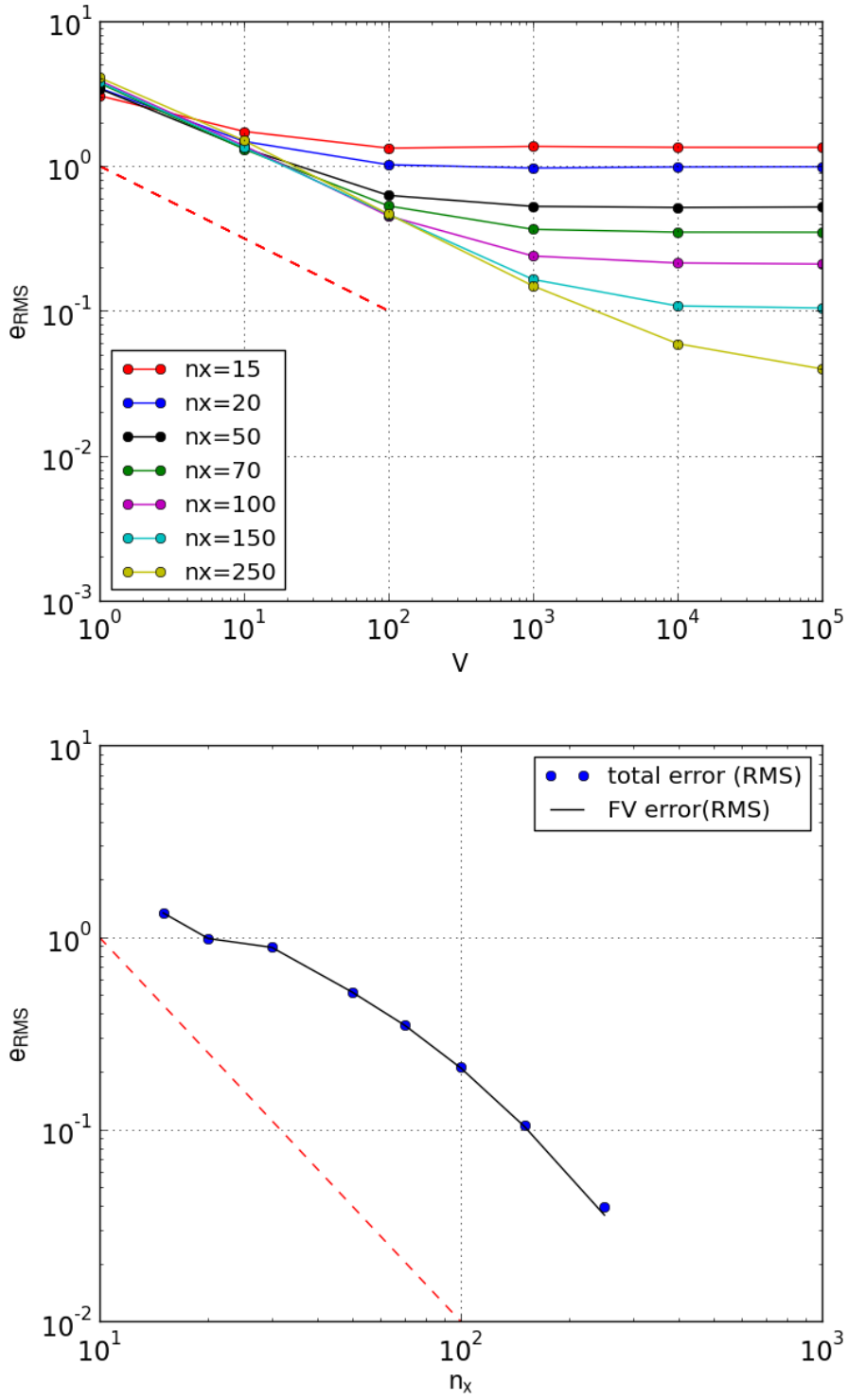

Figure 5.8: e_{RMS} variation with V and n_{x} for advection using Piecewise-linear scheme. Dashed line represents a line with slope of $(-1/2)$ in the figure on top and slope (-2) in figure in the bottom.

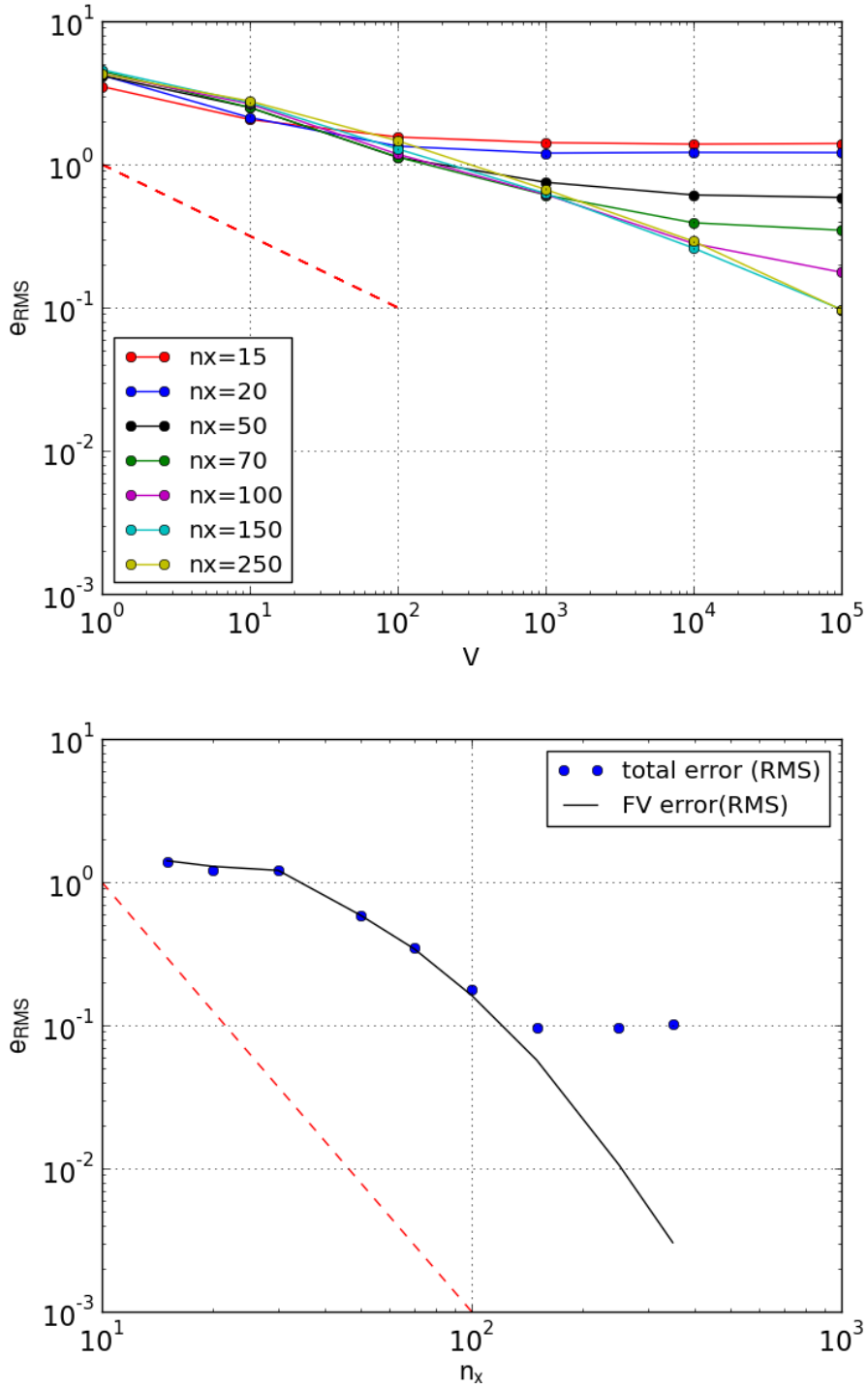

Figure 5.9: e_{RMS} variation with V and n_{x} for advection using RK-3 scheme. Dashed line represents a line with slope of $(-1/2)$ in the figure on top and slope (-3) in figure in the bottom.

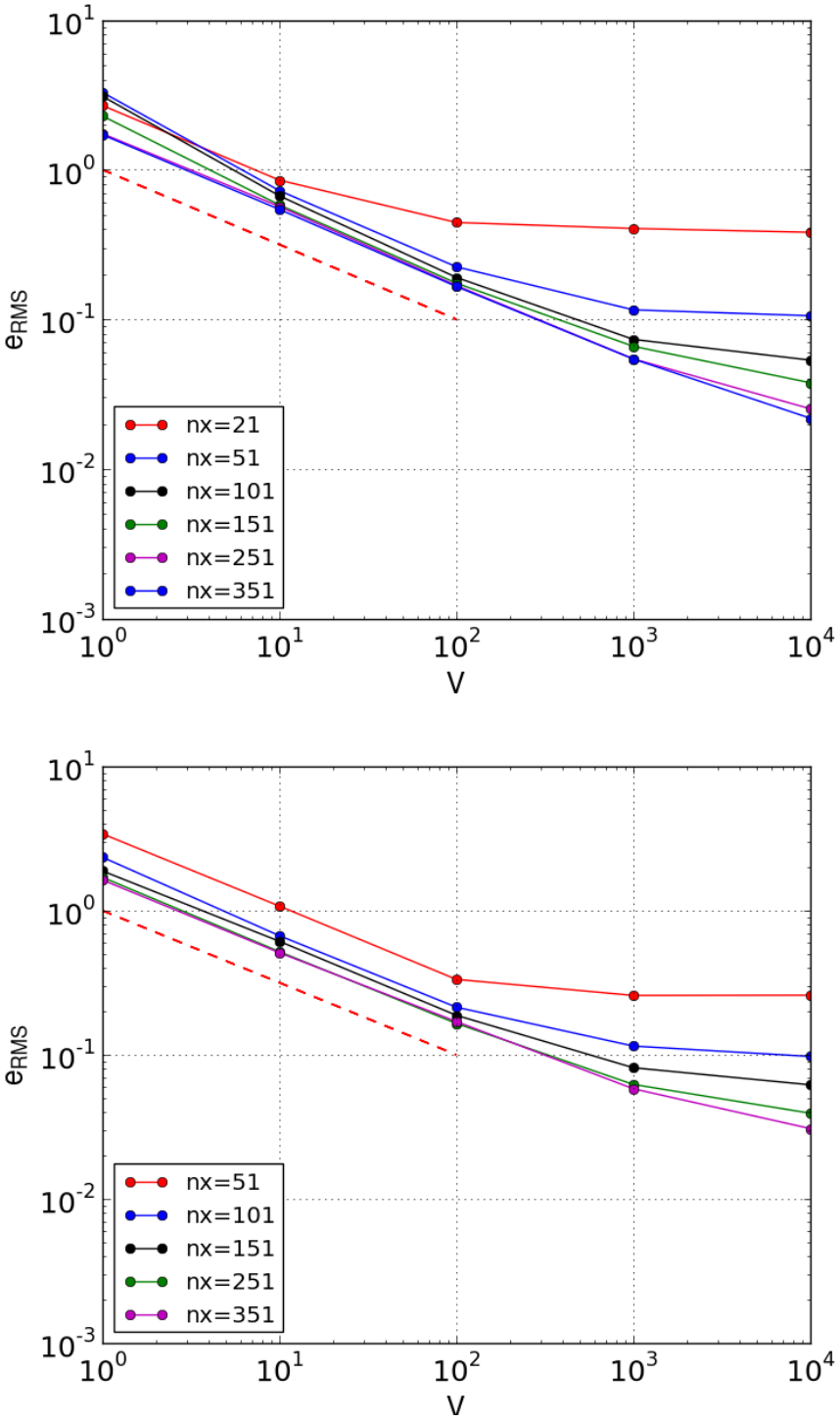

Figure 5.10: e_{RMS} variation with V for diffusion using second order(top) and fourth order scheme(bottom). Dashed line represents a line with slope of $(-1/2)$ on a loglog scale.

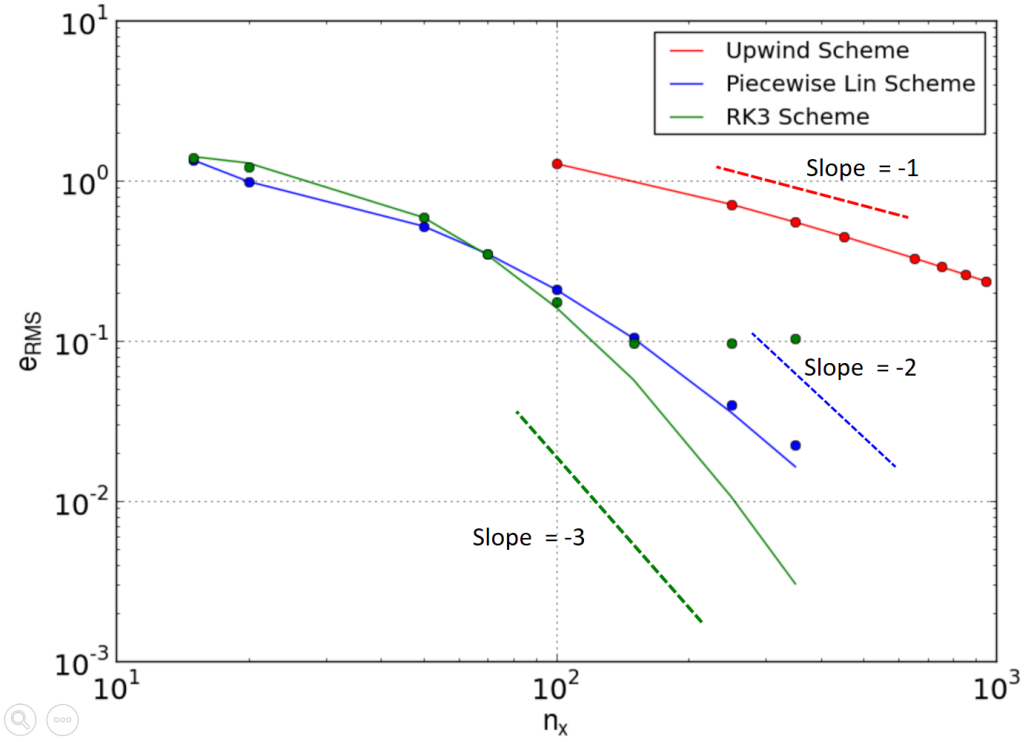

Figure 5.11: Convergence of e_{RMS} with grid size (n_{x}) for different advection schemes. The solid lines represent the FV error and bubbles represent the total RMS error for Upwind, Piecewise-lin and RK-3 schemes at $V = 10^4$, $V = 10^5$ and $V = 10^5$ respectively. The error plotted is the absolute error based on the same initial conditions for all schemes.

CHAPTER 6

CONCLUSIONS

6.1 Summary

This work describes an approach to model particle-resolved transport stochastically using higher-order methods. This work follows a sampling method for solving the advection-diffusion process of particles in a predefined velocity field and a given value of diffusion coefficient. In all the work, a uniform grid has been considered with staggered velocity values. The formulation started with passive scalar transport (PST) solution using finite-volume methods. Then flux-based stochastic transport (FBPT) was introduced by defining particle population movement in terms of particle flux and probabilities (Chapter 2). The coefficient matrix for flux calculation was split into the processes of advection (C_{adv}) and diffusion (C_{diff}). To keep the diffusion process random, even in a case of zero gradient, the diffusion coefficient matrix (C_{diff}) was further split into two parts. Since all the matrices are split from the same coefficient matrix of PST, the total particle concentration was expected to be the same as for finite-volume PST method results which was also theoretically proved in Theorem 1.

Since the formulation developed in the work is valid for any explicit schemes, different schemes can be used by changing the coefficient matrix C, which was discussed in Chapter 3. Numerical errors encountered were split into finite volume error and stochastic error (Chapter 4), and it was proved that the expected value of root-mean-square of the total error should depend on $1/\sqrt{V}$ in Theorem 3. This was confirmed numerically for 1D advection and diffusion tests as shown in Figures 5.7, 5.8, 5.9 and 5.10. The numerical results also verified the claim made in Theorem 2 that stochastic error diminishes when number of particle in a sample volume, V, increases. It is evident from the equation (4.2) that the total error becomes closer to

finite volume error, which was observed numerically in the flattening of the e_{RMS} vs V curve for large values of V. From all the aforementioned numerical results, it can be concluded that the transport results from FBPT model are close to the analytical solutions for the test cases and since the model is based on particle flux, it can be applied to WRF framework. In the case of a very high-grid resolution, the Upwind advection scheme is recommended because of its zero dispersion error. For cases where a high grid convergence is required, higher-order schemes, such as Piecewise linear or RK-3, can be used keeping in mind that some dispersion error will be introduced in the model. Although the second order diffusion was found sufficient for the modeling of test cases discussed in the work, a general formulation for a higher-order diffusion on a uniform grid was provided in the document.

6.2 Future Work

This work laid the foundation of stochastic methods for particle-resolved transport. It can be expanded in various ways. In particular, the momentum-coupling between fluid velocity and particle velocity was not considered in this work because of the insignificant masses of individual aerosol particles. The method can be modified to include more coupling equations to model transport of heavier particles such as sand. This method is useful for particles with diverse composition, and the composition has to be traced in the simulation.

Since only the transport is considered in the problem, and other chemical and physical processes of aerosols such as coagulation, condensation, dilution and deposition were to be modeled using operator splitting. As a precaution, the time scales of each of these processes should to be significantly different from each other to decouple the processes from each other.

The thesis work only discusses transport in 1-dimensional space. The approach can be applied to a 2D or a 3D Cartesian space with staggered uniform grid. As an example, Figure 6.1 shows advection results for a 2D rotating field [Takacs, 1985] applied to a cylindrical particle population distribution. Since the method only works for uniform structured-grids, method will have to be reformulated for non-uniform grids. The higher resolution results for uniform grids can be obtained by applying grid nesting [Skamrock, 1989],

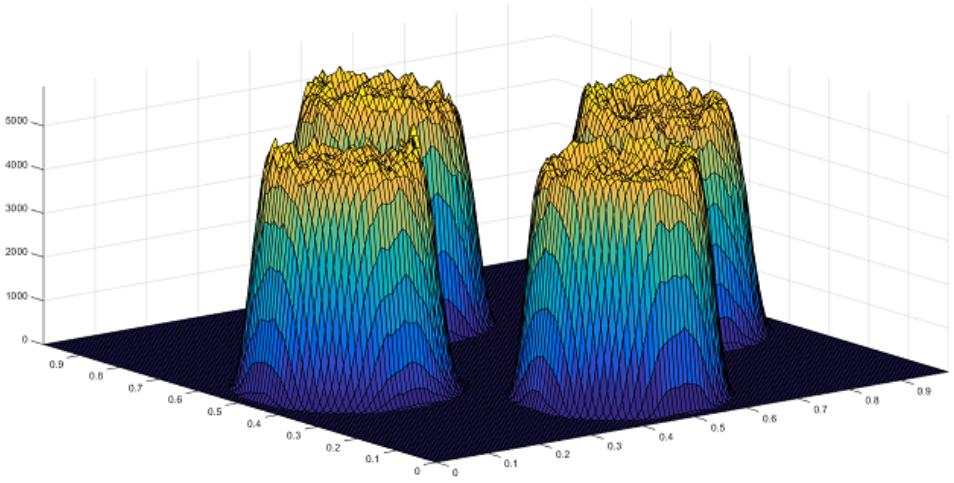

Figure 6.1: Particle concentration for $t = T/4$, $t = T/2$, $t = 3T/4$ and $t = T$ on a 2D simulation for a rotating flow and zero gradient boundary conditions. Here, T is the time taken for a particle to complete one revolution in the domain. Operator split technique in x any y directions was used for this simulation.

but it will require an additional sampling step for distributing particles in the nest.

This approach is compatible with the already existing finite-volume framework of WRF and it keeps track of individual particle composition during transport. Further work may include the integration of these methods with aerosol physical and chemical processes to acquire a fully functional aerosol modeling tool.

APPENDIX A

FINITE VOLUME METHODS

A.1 Flux based form for PST

A passive scalar transport equation with reaction part included is given by,

$$\frac{\partial q}{\partial t} = -\nabla \cdot (uq) + \nabla \cdot [D_0(\nabla q)] + S_V \tag{A.1}$$

$-u(\nabla q)$,$D_0(\nabla^2 q)$ and S_V are advection part, diffusion part and reaction/source part of the scalar equation respectively. Integrating these equations for a control volume,

$$\int_V \frac{\partial q}{\partial t} dV = \int_V [-\nabla \cdot (uq) + \nabla \cdot [D_0(\nabla q)]] dV + \int_V S_V dV$$
$$\int_V \frac{\partial q}{\partial t} dV = \int_V \nabla \cdot [-uq + D_0(\nabla q)] dV + \int_V S_V dV$$

Using Gauss Divergence theorem,

$$\int_V \frac{\partial q}{\partial t} dV = \oint_s [-(uq) + D_0(\nabla q)].n \; ds + \int_V S_V dV$$
$$\frac{\partial Q}{\partial t} dV = \triangle F + \int_V S dV \tag{A.2}$$

Where, $\triangle F$ represents the net flux exchange from the boundaries of control volume, Q represents the volume average of the scalar in the control volume(CV). A sample CV in Cartesian coordinates is shown in Figure A.1.

$$\triangle F = \underbrace{\oint_s [-(uq)] \cdot n \; dS}_{\text{Advection}} + \underbrace{\oint_s [D_0(\nabla q)] \cdot n \; dS}_{\text{Diffusion}} \tag{A.3}$$

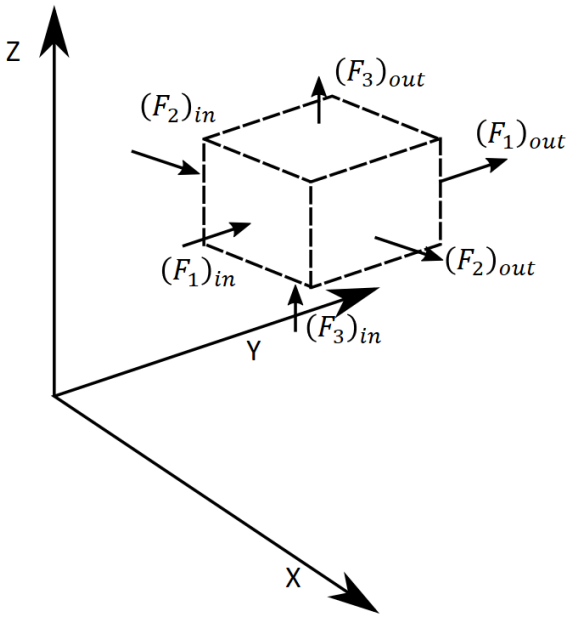

$$\Delta F = \sum_i (F_i)_{in} - \sum_i (F_i)_{out}$$

Figure A.1: A sample control volume in Cartesian coordinates.

The net flux for a scalar can be divided into advection and diffusion as shown in equation (A.3). The flux through a face due to advection depends on the velocity at the corresponding face, and the flux due to diffusion depends on the diffusion coefficient and the spatial gradient of scalar at the face.

REFERENCES

I J Ackermann, H Hass, M Memmesheimer, A Ebel, F S Binkowski, and U Shankar. Modal aerosol dynamics model for europe: Development and first applications. *Atmospheric environment*, 32(17):2981–2999, 1998.

K Adachi, S H Chung, and P R Buseck. Shapes of soot aerosol particles and implications for their effects on climate. *Journal of Geophysical Research: Atmospheres*, 115(D15), 2010.

B A Albrecht. Parameterization of trade-cumulus cloud amounts. *Journal of the Atmospheric Sciences*, 38(1):97–105, 1981.

ICEM CFD ANSYS. 11.0, CFD tool, ANSYS.

S E Bauer, D L Wright, D Koch, E R Lewis, R McGraw, L-S Chang, S E Schwartz, and R Ruedy. Matrix (multiconfiguration aerosol tracker of mixing state): an aerosol microphysical module for global atmospheric models. *Atmospheric Chemistry and Physics*, 8(20):6003–6035, 2008.

R W Bergstrom, P Pilewskie, P B Russell, J Redemann, T C Bond, P K Quinn, and B Sierau. Spectral absorption properties of atmospheric aerosols. *Atmospheric Chemistry and Physics*, 7(23):5937–5943, 2007.

F M Breon, Didier T, and S Generoso. Aerosol effect on cloud droplet size monitored from satellite. *Science*, 295(5556):834–838, 2002.

J E Castillo, J M Hyman, M Shashkov, and S Steinberg. Fourth-and sixth-order conservative finite difference approximations of the divergence and gradient. *Applied Numerical Mathematics*, 37(1):171–187, 2001.

USER CD-adapco. CFD tool: STAR-CCM+, 2009.

S H Chung and J H Seinfeld. Climate response of direct radiative forcing of anthropogenic black carbon. *Journal of Geophysical Research: Atmospheres*, 110(D11), 2005.

W P Crowley. NUMERICAL ADVECTION EXPERIMENTS 1. *Monthly Weather Review*, 96(1):1–11, 1968.

G T Csanady. *Turbulent diffusion in the environment*, volume 3. Springer Science & Business Media, 2012.

J H Curtis, M D Michelotti, N Riemer, M T Heath, and M West. Accelerated simulation of stochastic particle removal processes in particle-resolved aerosol models. *Journal of Computational Physics*, 322:21–32, 2016a.

J H Curtis, N Riemer, and M West. Coupling the stochastic particle-resolved aerosol model PartMC-MOSAIC with the WRF single column model: WRF-PartMC-MOSAIC-SCM. *Geoscientific Model Development Discussion*, 2016b.

D R Durran. *Numerical methods for wave equations in geophysical fluid dynamics*, volume 32. Springer Science & Business Media, 2013.

A Einstein. The theory of the brownian movement. *Ann. der Physik*, 17:549, 1905.

R Furth and A D Cowper. Investigations on the Theory of the Brownian Movement by Albert Einstein, 1956.

D T Gillespie. An exact method for numerically simulating the stochastic coalescence process in a cloud. *Journal of the Atmospheric Sciences*, 32 (10):1977–1989, 1975.

D T Gillespie. Exact stochastic simulation of coupled chemical reactions. *The journal of physical chemistry*, 81(25):2340–2361, 1977.

S L Gong, L A Barrie, J-P Blanchet, K Von Salzen, U Lohmann, G Lesins, L Spacek, L M Zhang, E Girard, H Lin, et al. Canadian aerosol module: A size-segregated simulation of atmospheric aerosol processes for climate and air quality models 1. module development. *Journal of Geophysical Research: Atmospheres*, 108(D1), 2003.

G A Grell, S E Peckham, R Schmitz, S A McKeen, G Frost, W C Skamarock, and B Eder. Fully coupled "online" chemistry within the WRF model. *Atmospheric Environment*, 39(37):6957–6975, 2005.

A Haghighat. *Monte Carlo Methods for Particle Transport*. Taylor & Francis, 2014. ISBN 9781466592537. URL `https://books.google.com/books?id=vcHrkwEACAAJ`.

D J Higham. An algorithmic introduction to numerical simulation of stochastic differential equations. *SIAM review*, 43(3):525–546, 2001.

B J Huebert and A L Lazrus. Bulk composition of aerosols in the remote troposphere. *Journal of Geophysical Research: Oceans*, 85(C12):7337–7344, 1980.

M Z Jacobson Chapter 5. *Air pollution and global warming: history, science, and solutions*. Cambridge University Press, 2012.

R K Jain. An efficient multinomial sampling algorithm for spatially distributed stochastic particle simulations. *IDEALS*, 2011.

A Jaruga, S Arabas, and H Pawlowska. Super-droplet method as a versatile numerical approach for representing aerosol-cloud-aerosol interactions. In *EGU General Assembly Conference Abstracts*, volume 15, page 2284, 2013.

H Jasak. Openfoam: open source cfd in research and industry. *International Journal of Naval Architecture and Ocean Engineering*, 1(2):89–94, 2009.

S Lampoudi, D T Gillespie, and L R Petzold. The multinomial simulation algorithm for discrete stochastic simulation of reaction-diffusion systems. *The Journal of chemical physics*, 130(9):094104, 2009.

J J McCarthy. *Climate change 2001: impacts, adaptation, and vulnerability: contribution of Working Group II to the third assessment report of the Intergovernmental Panel on Climate Change*. Cambridge University Press, 2001.

Z Meng, D Dabdub, and J H Seinfeld. Size-resolved and chemically resolved model of atmospheric aerosol dynamics. *Journal of Geophysical Research: Atmospheres*, 103(D3):3419–3435, 1998.

P Moin. *Engineering numerical analysis*. Cambridge University Press Cambridge, UK, 2001.

M Müller, D Charypar, and M Gross. Particle-based fluid simulation for interactive applications. In *Proceedings of the 2003 ACM SIGGRAPH/Eurographics symposium on Computer animation*, pages 154–159. Eurographics Association, 2003.

S E Peckham, G A Grell, S A McKeen, M Barth, G Pfister, C Wiedinmyer, J D Fast, W I Gustafson, S J Ghan, R A Zaveri, et al. *WRF/Chem Version 3.3 User's Guide*. US Department of Commerce, National Oceanic and Atmospheric Administration, Oceanic and Atmospheric Research Laboratories, Global Systems Division, 2012.

C Pilinis and X Li. Particle shape and internal inhomogeneity effects on the optical properties of tropospheric aerosols of relevance to climate forcing. *Journal of Geophysical Research: Atmospheres*, 103(D4):3789–3800, 1998.

C J Pope and J B Howard. Simultaneous particle and molecule modeling (SPAMM): An approach for combining sectional aerosol equations and elementary gas-phase reactions. *Aerosol science and technology*, 27(1):73–94, 1997.

C A Pope III, M Ezzati, and D W Dockery. Fine-particulate air pollution and life expectancy in the united states. *New England Journal of Medicine*, 360(4):376–386, 2009.

H Resat, L Petzold, and M F Pettigrew. Kinetic modeling of biological systems. *Computational Systems Biology*, pages 311–335, 2009.

N Riemer, M West, R A Zaveri, and R C Easter. Simulating the evolution of soot mixing state with a particle-resolved aerosol model. *Journal of Geophysical Research: Atmospheres*, 114(D9), 2009.

N Riemer, M West, R Zaveri, and R Easter. Estimating black carbon aging time-scales with a particle-resolved aerosol model. *Journal of Aerosol Science*, 41(1):143–158, 2010.

J H Seinfeld and S N Pandis. *Atmospheric chemistry and physics: from air pollution to climate change*. John Wiley & Sons, 2012.

S Shima, K Kusano, A Kawano, T Sugiyama, and S Kawahara. The super-droplet method for the numerical simulation of clouds and precipitation: A particle-based and probabilistic microphysics model coupled with a non-hydrostatic model. *Quarterly Journal of the Royal Meteorological Society*, 135(642):1307–1320, 2009.

C W Shu. *Essentially non-oscillatory and weighted essentially non-oscillatory schemes for hyperbolic conservation laws*. Springer, 1998.

W C Skamrock. Truncation error estimates for refinement criteria in nested and adaptive models. *Monthly weather review*, 117(4):872–886, 1989.

P Stier et al. Mechanistic aerosol-cloud coupling and indirect aerosol effects in the aerosol-climate model echam-ham, 2012.

L L Takacs. A two-step scheme for the advection equation with minimized dissipation and dispersion errors. *Monthly Weather Review*, 113(6):1050–1065, 1985.

U M Titulaer. A systematic solution procedure for the fokker-planck equation of a brownian particle in the high-friction case. *Physica A: Statistical Mechanics and its Applications*, 91(3):321–344, 1978.

S Twomey. Aerosols, clouds and radiation. *Atmospheric Environment. Part A. General Topics*, 25(11):2435–2442, 1991.

A S Wexler, F W Lurmann, and J H Seinfeld. Modelling urban and regional aerosols—i. model development. *Atmospheric Environment*, 28(3):531–546, 1994.

E R Whitby and P H McMurry. Modal aerosol dynamics modeling. *Aerosol Science and Technology*, 27(6):673–688, 1997.

K T Whitby and B Cantrell. Atmospheric aerosols- characteristics and measurement. In *International Conference on Environmental Sensing and Assessment, Las Vegas, Nev*, page 1, 1976.

L J Wicker and W C Skamarock. Time-splitting methods for elastic models using forward time schemes. *Monthly Weather Review*, 130(8):2088–2097, 2002.

X Yang, C Zhao, L Zhou, Y Wang, and X Liu. Distinct impact of different types of aerosols on surface solar radiation in china. *Journal of Geophysical Research: Atmospheres*, 2016.

R A Zaveri, R C Easter, J D Fast, and L K Peters. Model for simulating aerosol interactions and chemistry (MOSAIC). *Journal of Geophysical Research: Atmospheres*, 113(D13), 2008.

R A Zaveri, J C Barnard, R C Easter, N Riemer, and M West. Particle-resolved simulation of aerosol size, composition, mixing state, and the associated optical and cloud condensation nuclei activation properties in an evolving urban plume. *Journal of Geophysical Research: Atmospheres*, 115(D17), 2010.

Y Zhang, C Seigneur, J H Seinfeld, M Z Jacobson, and F S Binkowski. Simulation of aerosol dynamics: A comparative review of algorithms used in air quality models. *Aerosol Science & Technology*, 31(6):487–514, 1999.